ACS APPLIED MATERIALS & INTERFACES

www.acsami.org

Research Article

A Triple-Site Gd_3 Carborane Metal–Organic Framework toward Scalable Quantum Computing

Elena Bartolomé,* Xiao-Bao Li, Ana Arauzo, Javier Luzón, Inés García-Rubio, and José Giner Planas*

Cite This: https://doi.org/10.1021/acsami.5c06002

Read Online

ACCESS | Metrics & More | Article Recommendations | Supporting Information

ABSTRACT: Metal–organic frameworks (MOFs) incorporating arrays of molecular spin qubits (quMOFs) offer a promising pathway toward scalable quantum computing. In this work, we introduce a novel quMOF, $\{[(Gd)_3(m\text{CB-L})_4(NO_3)(DMF)_x]_n \cdot Solv\}$, constructed with a carborane linker and Gd(III) ions at three distinct coordination sites. We thoroughly characterize its magneto-thermal properties using dc/ac magnetometry, X-ray absorption spectroscopy, X-ray magnetic circular dichroism, and heat capacity measurements. The quantum computing potential is demonstrated through ab initio calculations and pulsed electron paramagnetic resonance on GdY-diluted analogues, revealing T_m = 0.7 μs and Rabi oscillations persisting up to 50 K. Each of the three isolated Gd(i) sites in GdY-MOFs functions as an 8-level qudit, accessible via X-band transitions. Notably, the triple-site Gd_3 quMOF provides an unprecedented qudit with $d = (2S + 1)^3 = 512$ states, capable of encoding up to 9 qubits, marking a significant advance in the scalability of molecular-based quantum computing systems.

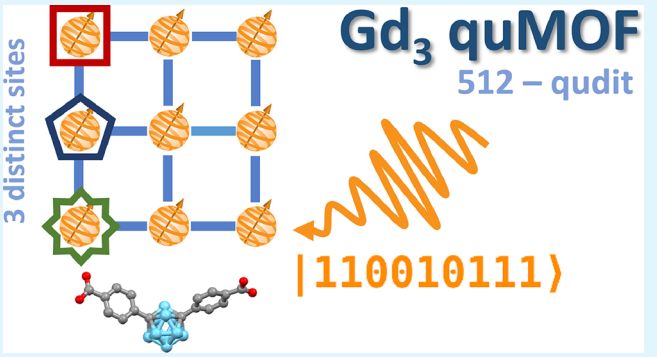

KEYWORDS: *lanthanide metal–organic framework, gadolinium, carborane-linker, molecular qubits, qudit, quantum computing*

INTRODUCTION

Quantum Computing (QC) has emerged as a revolutionary quantum technology that promises to transform numerous fields by solving complex problems that surpass the capabilities of classical supercomputers, with foreseen application in artificial intelligence (AI), machine learning, optimization, data analysis, and beyond.[1,2] The basic unit of QC is the qubit, which represents a coherent superposition of two states ("0" and "1"). Various qubit platforms have been proposed to date, including superconducting circuits,[3] quantum dots,[4] trapped ions,[5] neutral atoms, diamond vacancies, photons,[6] topological qubits and molecules, each offering distinct strengths and challenges.[7,8]

Among these, molecular spin qubits present interesting advantages.[9] Molecules are inherently quantum systems with discrete energy levels that can be finely tuned through chemical design. The bottom-up synthetic approach enables the scalable and reproducible production of identical qubits, pushing miniaturization to its limits. Furthermore, molecular qubits can be functionalized, deposited on diverse surfaces, or assembled into periodic arrays, providing exceptional flexibility for integration into quantum devices. The electron and nuclear spin state of these systems can be manipulated using microwave (MW) or radio frequency pulses, respectively, facilitating the operation of quantum gates ("qugates") and algorithm execution. Advances in decoherence mitigation have led to molecules exhibiting coherence times as long as $T_2 \sim 1$ ms at 10 K, as demonstrated in the vanadium monomer $((d_{20}\text{-}Ph_4P)_2[V(C_8S_8)_3])$.[10] Since 2016, interest has increasingly shifted toward lanthanide-based qubits, where tailored crystal fields enable the design of the desired quantum states. Molecules like bis(phthalocyanine)terbium(III) ($TbPc_2$)[11] have already demonstrated compliance with DiVincenzo's criteria for qubits,[12] showing well-defined energy levels, scalability, long coherence times, efficient initialization, manipulation, readout, and capability for universal gate implementation. Recent progress has even enabled quantum error correction (QEC) within single lanthanide molecules,[13] further underscoring their promise for quantum information processing.

Current research focuses on overcoming key challenges for the practical implementation of molecular qubits in QC,[8,14] such as integrating and coupling molecules into hybrid solid-state devices,[9,15−17] developing optically addressable molecular spins,[18,19] and expanding the dimension of the accessible

Received: March 25, 2025
Revised: June 3, 2025
Accepted: June 4, 2025

Hilbert space.[20] Scaling up the number of states is essential to boost computational power and enable advanced quantum algorithms, thereby unlocking the true potential of QC.

Scaling can be achieved through two fundamentally distinct approaches. The first involves combining multiple two-level qubits within a molecular system. This can be achieved by integrating several qubits within a single molecule, as demonstrated with heterometallic lanthanide-based [LnLn'][21,22] and [LnLn'Ln][13,23] qugates, or by connecting molecular qubits through supramolecular chemistry, such as in Cr_7Ni systems.[24] The second approach leverages the internal states of magnetic molecules to access a greater number of quantum transitions within a *d*-level quantum system, known as a "qudit". A single *d*-level qudit can efficiently encode *N* two-level qubits ($d = 2^N$). Using qudits instead of conventional two-level qubits allows for more compact quantum architectures, the implementation of simplified or improved quantum algorithms[25,26] and facilitates QEC protocols.[13,27,28] Thus, qudits can significantly boost quantum logic in applications ranging from quantum computing,[29] quantum sensing,[30] and quantum simulation.[31,32]

Molecular 4-level qudits have been successfully realized in $TbPc_2$ using the $I = 3/2$ nuclear spin of Tb(III),[33] which enabled the first demonstration of Grover's algorithm,[11,34] while the coupling of two Tb-qudits allowed creating a 16-level system in Tb_2Pc_3.[35] Gd(III) ion with a large spin $S = 7/2$ and no orbital contribution ($L = 0$), offers the possibility of producing qudits of larger dimensionality. The sensitivity of Gadolinium magnetic anisotropy to the local coordination gives rise to zero-field splittings, which can be used to shape qudits.[36−39] Following this idea, a single-ion $[GdW_{30}]$ $d = 8$ qudit (equivalent to $N = 3$ qubits) was reported,[40] and more recently, the synthesis of a dissymmetric [GdGd'] molecule allowed to build up a $d = 64$ qudit, hosting up to $N = 6$ addressable spin qubits.[41] This is the highest number of qubits achieved in molecular QC so far.

Interestingly, Metal−Organic Frameworks (MOFs), composed of organic linkers and metal ions arranged in crystalline porous structures, provide ideal platforms to organize qubits into ordered arrays. These so-called "quMOFs" are promising for QC, enabling scalable and modular qubit structures, while allowing precise control over qubit spacing and magnetic dilution to reduce decoherence. Their porosity also supports quantum sensing[42−47] and enables customization through guest inclusion.[48] Qubits have been integrated into MOFs as paramagnetic metal centers in the nodes (e.g., Cu^{2+} for sensing[49]), metal centers within the building ligands,[50−52] or as organic radicals.[42−47]

In particular, MOFs coordinating lanthanide (Ln) ions stand out for their unique magnetic, electronic and optical properties, making them promising materials for QC as well as for applications in magnetic refrigeration, luminescence, or catalysis. However, so far, only three Ln(III) quMOFs have been reported for QC: (i) the Gd(III)-based 3D MOF, $[Gd(bipyNO)_4](TfO)_3{\cdot}x$MeOH, where pulsed electron paramagnetic resonance (EPR) experiments on a diluted analogue revealed a spin−spin relaxation time $T_m = 612$ ns and a spin−lattice relaxation time $T_1 = 66$ μs at 3.5 K, along with Rabi oscillations up to 40 K;[53] (ii) the 2D $Gd^{III}Na^{I}$-based oxamato supramolecular coordination framework, with extended relaxation times ($T_m = 4.25$ μs at 8 K and $T_1 = 1.66$ ms at 4 K) in a 0.12% magnetically diluted sample;[54] and (iii) layered MOF $[N(C_2H_5)_4][Ln_xLa_{100-x}(CAN)_2(H_2O)]$, Ln = Gd(III), Nd(III), with $T_m \approx 2$ μs at 3.2 K in 0.1−0.5% diluted samples.[55] We note that Gd(III)-based MOFs are also attractive candidates for low-temperature magnetic cooling,[16−18] due to their large magnetocaloric effect (MCE), which is based on Gd spin-only $S = 7/2$ (maximum entropy can be obtained from $S_{max} = R\ln(2S + 1)$). The MCE performance of 4f compounds of various dimensions, including Gd 3D MOFs, has been recently reviewed.[19]

Recently, some of us reported the one-pot synthesis of a family of lanthanide MOFs using the carborane linker *m*CB-L = 1,7-di(4-carboxyphenyl)-1,7-dicarba-*closo*-dodecarborane,[56] with the general formula $\{[(Ln)_3(mCB\text{-}L)_4(NO_3)(DMF)_x]_n{\cdot}Solv\}$. Icosahedral carboranes are a class of commercially available, stable boron-rich clusters[57−59] known for their high hydrophobicity[60−66] and unusual electronic structure, often regarded as inorganic 3D "aromatic" analogs of arenes.[57−59] The steric bulkiness and acidity of the *m*CB-L linker facilitate the synthesis of multivariate MOFs incorporating any desired combination of lanthanides, enabling the exploration of complex magnetic materials and multifunctional materials with tailored properties.[67] In previous studies, we highlighted the multifunctional properties of Tb, Dy MOFs,[68] mixed Tb/Eu MOFs with exceptional luminescence,[56] "self-refrigerated" GdLn (Ln = Tb, Dy, Eu) MOFs,[69] and the first MOF incorporating eight different-sized rare-earth ions.[67] The MOF structures, which are all isostructural, are formed by the repetition of Secondary Building Units (SBUs) containing three ions in distinct coordination environments, while the bulky carborane ligands separate adjacent chains to create the 3D architecture.

Importantly, the ability to create multilanthanide MOFs with distinct coordination sites opens promising possibilities for scaling the Hilbert space for QC. Notably, a Gd_3 quMOF with three distinct sites could yield an unparalleled qudit with $d = (2S + 1)^3 = 512$ states, equivalent to 9 two-level qubits, providing an exceptional platform for scaling Quantum Computing systems.

In this work, we report the synthesis and characterization of a triple-site Gd(III) carborane-based MOF, $\{[(Gd)_3(mCB\text{-}L)_4(NO_3)(DMF)_x]_nSolv\}$, along with two magnetically diluted analogs. We first investigate its magneto-thermal properties using dc/ac magnetometry, XAS-XMCD, and heat capacity measurements. Second, we assess the quantum computing potential of these multisite Gd quMOFs through ab initio calculations and pulsed EPR experiments, highlighting their capacity to expand the Hilbert space.

RESULTS AND DISCUSSION

Synthesis and Structure. For this work, we synthesized the carborane-based Gd(III) MOF (***m*CB-Gd**) and two magnetically diluted analogs, ***m*CB-Gd$_{0.08\%}$** and ***m*CB-Gd$_{1.76\%}$**, containing 0.08% and 1.76% Gd in Yttrium, respectively, using a simple one-pot method previously applied to the preparation of other Ln-based MOFs in the same family.[67] Powder X-ray diffraction (PXRD) data confirms that these materials are isostructural with previously reported *m*CB-Ln MOFs (Figure S1),[56,67−69] although with clear preferred orientation effects resulting from the highly anisotropic crystalline materials. The metals' content in the mixed MOFs was determined by Inductively Coupled Plasma−Mass Spectrometry (ICP-MS), as detailed in the Experimental Section.

https://doi.org/10.1021/acsami.5c06002
ACS Appl. Mater. Interfaces XXXX, XXX, XXX−XXX

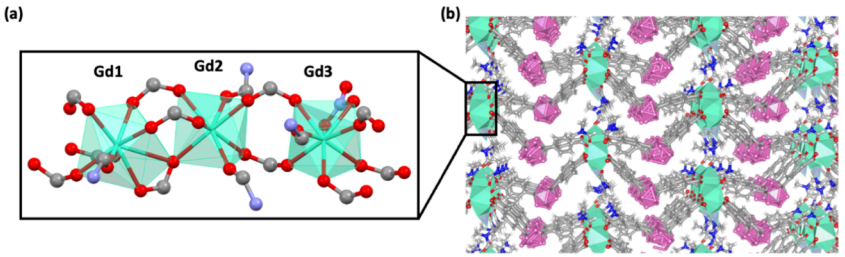

Figure 1. Representation of the crystal structure for ***m*CB-Gd**. (a) Detail of the Secondary Building Unit (SBU) containing three nonequivalent sites for Gd(III): Gd(1), Gd(2), Gd(3). (b) View of the 3D structure showing the coordination of *m*CB-L to Gd atoms. Green polyhedra represents the Gd coordination spheres. H atoms are omitted for clarity. Color code: B, pink; C, gray; O, red; N, blue.

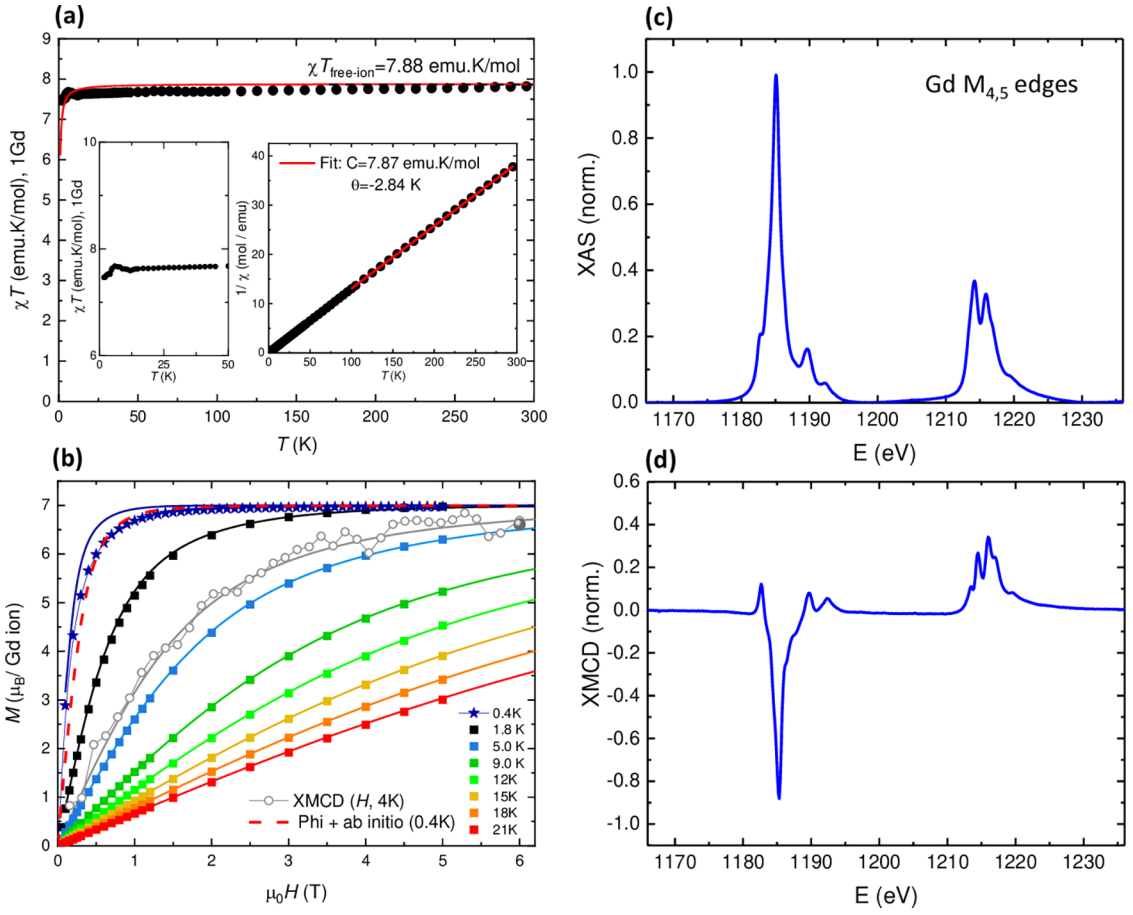

Figure 2. Dc magnetic properties of ***m*CB-Gd.** (a) χT product as a function of the temperature at 0.1 T per Gd ion, and zoom of the low-T region. Red line: simulation using ab initio-calculated parameters. Right inset: $1/\chi$ plot and Curie fit above 100 K. (b) Field-dependence of the magnetization, per Gd ion, at different applied temperatures between 0.4 to 21 K. Open circles represent the total magnetic moment per ion, $m_{TOT}(H)$, determined from XMCD measurements at T = 4 K. Bold circle: m_{TOT} value obtained from sum rules at 6 T, 4 K. Solid lines represent the theoretical Brillouin prediction for noninteracting Gd(III) ions with g = 2 and no anisotropy (D = 0). Red dashed line: *Phi* simulation of the 0.4 K curve using ab initio-calculated parameters. (c) Normalized, background-subtracted XAS and (d) XMCD spectra measured for ***m*CB-Gd** at Gd $M_{4,5}$ edges, at 6 T and 4 K.

Figure 1 shows a representation of the structure for ***m*CB-Gd**. The secondary building unit (SBU) of this MOF is formed by three nonequivalent Gd(III) ions —denoted Gd(1), Gd(2), Gd(3) —linearly arranged along the *a*-axis and capped by bridging or chelate-bridging *m*CB-L, chelate NO_3^- and DMF molecules. The coordination environment of Gd2 is composed of seven O atoms, while Gd1 and Gd3 are octa-coordinated by O atoms (Figure 1a).

Magnetic Properties. The static magnetic characterization of ***m*CB-Gd** is shown in Figure 2. The temperature-dependence of the χT product at 300 K reaches a value of 7.81 emu K/mol, very close to the free-ion value of 7.88 emu K/mol expected for one Gd(III) with S = 7/2 and g = 2.0 (Figure 2a). By decreasing the temperature, the χT value remains nearly constant down to 50 K, and it only drops to a value of 7.46 emu K/mol at 1.8 K, as a result of the combined effect of very weak magnetic interactions between the Gd(III) ions and single ion magnetic anisotropy (*vide infra* ab initio calculations). The linear fit of the $1/\chi$ plot at high temperatures yields a Curie–Weiss temperature of θ = −2.84 K, pointing to the existence of overall antiferromagnetic (AF)

https://doi.org/10.1021/acsami.5c06002
ACS Appl. Mater. Interfaces XXXX, XXX, XXX−XXX

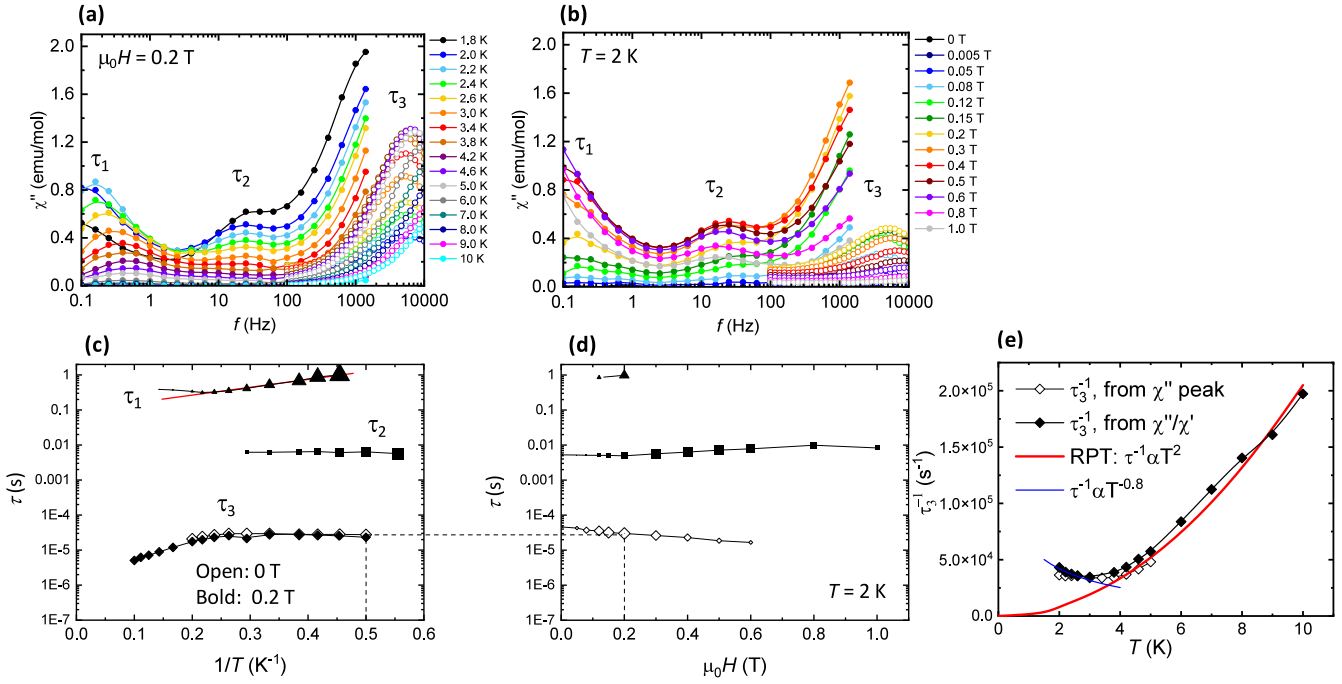

Figure 3. Spin−lattice magnetic relaxation of ***m*CB-Gd.** Top: Imaginary component of the ac susceptibility as a function of the frequency, $\chi''(f)$, of ***m*CB-Gd** MOF, (a) at μ_0H = 0.2 T and different temperatures, and (b) at T = 2 K under different applied magnetic fields. Data in the 0.1−10^3 Hz range (solid symbols) were obtained using a SQUID magnetometer, while data in the 10^2−10^4 Hz range (open symbols) were acquired with a PPMS. Bottom: (c) Magnetic relaxation time τ as a function of the inverse temperature at μ_0H = 0.2 T, and (d) as a function of the applied magnetic field at T = 2 K, for the different relaxation processes observed; (e) temperature dependence of the relaxation rate $\tau_3^{-1}(T)$: fit to a power-law $\tau_3^{-1} = KT^2$, where K = 2050 s^{-1} K^{-2}, between 4−10 K attributed to RPT (red line), and reciprocating thermal behavior, $\tau_3^{-1} \propto T^{-0.8}$, below 3 K (blue line).

interactions. In view of ab initio results, these AF interactions are mostly of dipolar origin.

The field-dependence of the magnetization curves of ***m*CB-Gd** at different temperatures are shown in Figure 2b. The $M(H)$ measured between 1.8 and 21 K are well fit by the theoretical Brillouin prediction for noninteracting Gd(III) ions with S = 7/2, g = 2. At very low temperatures, 0.4 K, the magnetization saturates at 7 μ_B at 5 T, but the $M(H)$ curve falls below the Brillouin prediction, indicating the presence of weak AF interactions and/or anisotropy. Notably, the experimental data at 0.4 K could be well fit within *Phi* code,[70] using the single-ion anisotropy (D_i) and orthorhombic (E_i) parameters for the three distinct Gd(i) sites, along with the interaction constants (J_{ij}) calculated by ab initio methods (*vide infra*, Table Figure 5a). The same model also satisfactorily fits the $\chi T(T)$ data (Figure 2a, red line).

To further characterize the material, ***m*CB-Gd** was analyzed using X-ray absorption spectroscopy (XAS) and X-ray magnetic circular dichroism (XMCD). Figure 2c,d shows the XAS and XMCD spectra measured at 4 K under a magnetic field of 6 T at the Gd $M_{4,5}$ edges. The XAS spectral features are characteristic of Gd(III), with the M_5 edge displaying a shoulder at 1182.8 eV, a main peak at 1185.1 and two satellites at 1189.4 and 1192.3 eV. The M_4 edge exhibits two peaks at 1214.2 and 1215.8 eV, along with a shoulder at 1219.2 eV. We determined the orbital (m_L), spin (m_s) and total magnetic moment ($m_{TOT} = m_L + m_s$) per Gd(III) ion in the sample from the XAS-XMCD spectra using the corrected sum rules for lanthanides,[24,25] yielding m_L = 0.16 ± 0.01 μ_B/ion, m_S = 6.47 ± 0.25 μ_B/ion and m_{TOT} = 6.61 ± 0.4 μ_B/ion. The field-dependence of the total magnetic moment, $m_{TOT}(H)$, was obtained by following the intensity of the XMCD(H) peak at the M_5 edge between −6 and 6 T, and scaling the curve with the value of m_{TOT} at 6 T. As shown in Figure 2b, the resulting curve agrees well with the Brillouin expectation at 4 K.

The exceptional hydrophobic properties of carborane linkers, along with the stability of our material in both water and organic solvents, enable the preparation of suspensions, facilitating the deposition of the material onto various technical surfaces.[56] For this study, a methanol suspension of ***m*CB-Gd** was prepared and drop-casted onto a Si substrate. Optical images show intact crystallites of ***m*CB-Gd** deposited on the Si substrate (Figure S2a). The XAS and XMCD spectra of the on-surface deposited ***m*CB-Gd**/Si, shown in Figure S2b,c, exhibit the same features as the bulk material. The spin, orbital, and total magnetic moments at 6 T, as well as the $m_{TOT}(H)$ curve, match the expected values for the sample at T = 4.6 K (Figure S2d). These results confirm that the magnetic properties of the ***m*CB-Gd** MOF are preserved after methanol-dispersion and surface deposition.

The dynamic magnetic properties of ***m*CB-Gd** were characterized by ac susceptibility measurements. Figure 3a shows the out-of-phase component of the susceptibility as a function of the frequency, $\chi''(f, T)$, at a constant applied magnetic field (μ_0H = 0.2 T) and temperatures between 1.8 and 20 K, while Figure 3b shows $\chi''(f, H)$ curves at a fixed temperature (T = 2.0 K) and varying magnetic fields in the 0−1 T range. From these data, three distinct spin relaxation processes are identified, with relaxation times labeled τ_1, τ_2 and τ_3. Figure 3c,d illustrate the dependence of the relaxation time on the inverse temperature, $\tau(1/T)$, and the magnetic field, $\tau(H)$, for each process.

https://doi.org/10.1021/acsami.5c06002
ACS Appl. Mater. Interfaces XXXX, XXX, XXX−XXX

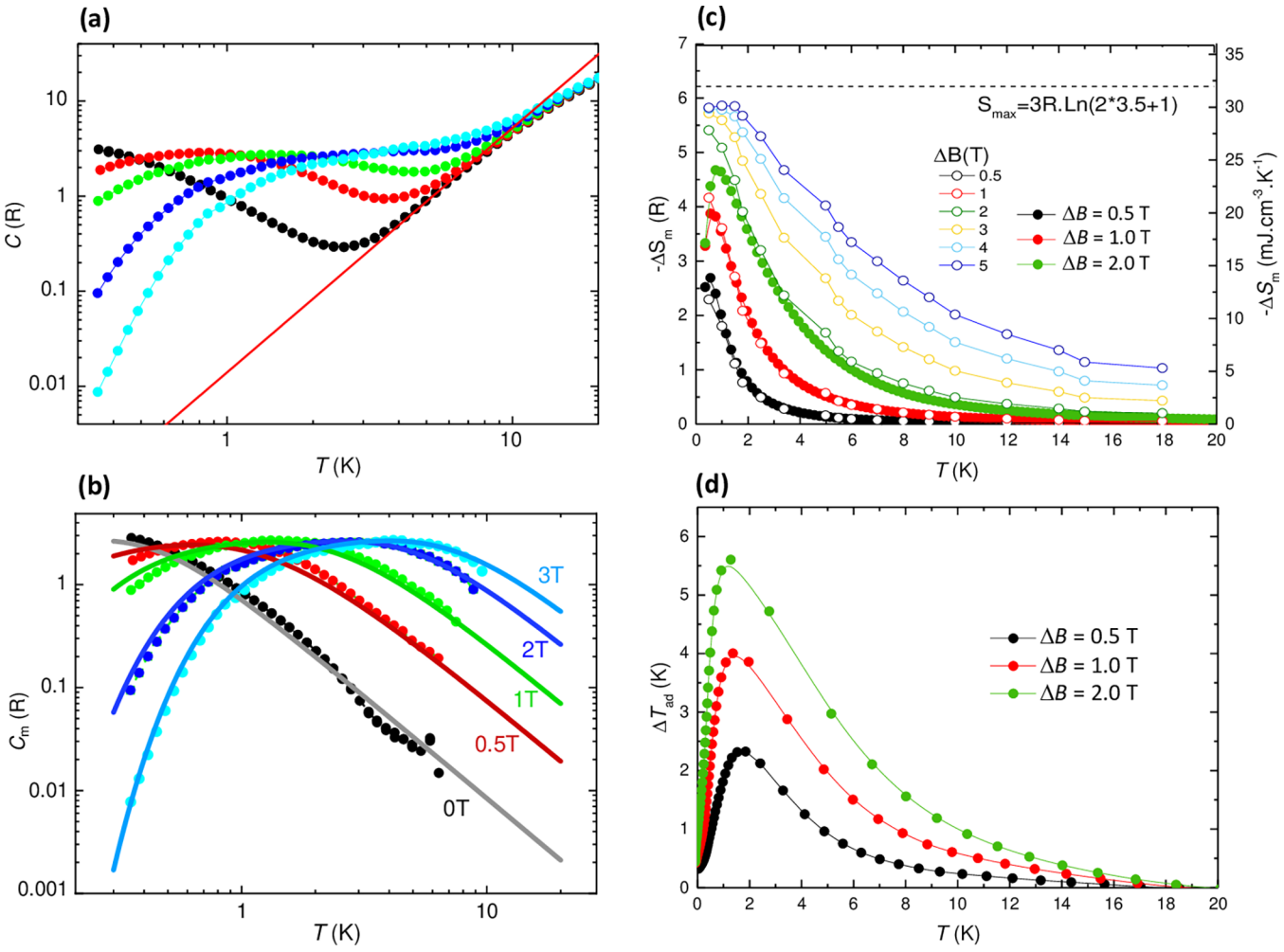

Figure 4. Specific heat and MCE of ***m*CB-Gd** quMOF. (a) Specific heat as a function of temperature at the indicated magnetic fields, $C(T,H)$. Red line: lattice contribution, $C_L = AT^n$, with $A = 1.4 \times 10^{-2}$ R·K$^{-2.57}$, n = 2.57. (b) Magnetic contribution to the specific heat, $C_m(T,H)$, and calculated curves using *Phi* code, and ab initio-derived single-ion D, E, parameters and J_{ij} coupling constants (Table in Figure 5a). (c) Temperature dependence of the magnetic entropy change, $-\Delta S_m$, obtained from HC measurements for applied magnetic field changes ΔB = 0.5, 1, 2 T (bold symbols), and from the $M(H)$ isotherms shown in Figure 2a, for ΔB = 0−5 T (open symbols). The dashed line represents the maximum available entropy for this system, $S_m = 3R\ln(2S + 1) = 6.24$ R, with $S = 7/2$; (d) temperature dependence of the adiabatic temperature change, $\Delta T_{ad}(T)$, obtained from HC for the indicated magnetic field changes ΔB.

The relaxational behavior of Gd(III) differs from that of orthodox single-ion magnets (SIMs), since the anisotropy energy due to zero-field-splitting (ZFS) in Gd is small, $\Delta_{ZFS}/k_B \approx |D|(S^2 - 1/4)$, with $S = 7/2$. In this case, based on the ab initio-calculated anisotropy values for the three distinct Gd(i) sites (Figure 5a), the expected ZFS anisotropy values are $\Delta_{ZFS}/k_B \approx 0.99$ K (Gd1), 1.42 K (Gd2) and 0.65 K (Gd3). These values are comparable to the Zeeman splitting (Δ_H/k_B = 1.9 K for $M_s = 7/2$ at $\mu_0 H$ = 0.2 T).

The first, slowest relaxation process has a relaxation time on the order of $\tau_1 \approx 0.1$ to 1 s. The $\tau_1(1/T)$ dependence at 0.2 T was fit to an Arrhenius law, with an activation energy of U/k_B = 5.2 K, consistent with the level splitting. Similar field-induced relaxation processes in Gd compounds have been earlier reported under comparable applied dc fields, such as the cyanoacetate complex $\{[Gd_2(CNCH_2COO)_6(H_2O)_4]\cdot 2H_2O\}_n$ (U/k_B = 5.5 K at 0.2 T),[71] or $[phen_2Gd_2(HCOO)_4(HCOO)_{2-2x}(NO_3)_{2x}]$ at 0.275 T.[72]

The second relaxation process ($\tau_2 \approx 0.006$ s) is nearly independent of temperature and magnetic field. A cross-relaxation mechanism mediated by spin−spin interactions may be hypothesized; however, the origin of this process remains unclear, and we therefore refrain from making a definitive assignment at this stage.

The third relaxation process (τ_3) is temperature-dependent, but cannot be attributed to an Orbach mechanism, as the effective energy barrier extracted from the ln τ_3 vs $1/T$ plot at 10 K (≈12.1 K) is an order of magnitude larger than the known anisotropy barrier. However, the relaxation rate τ_3^{-1} follows a T^2 dependence in the 4−10 K range (Figure 3e), consistent with a Resonant Phonon Trapping (RPT) mechanism.[71,73,74] RPT is a specific type of phonon-bottleneck effect in which phonons resonant with the spin transition energy become trapped near spin centers through repeated emission and reabsorption. These trapped phonons form quasi-coherent states whose energy cannot efficiently dissipate into the thermal reservoir, thereby delaying spin−lattice relaxation. For RPT to occur, two main conditions must be met, both of which are satisfied by ***m*CB-Gd**: (i) The magnetic coupling between spin centers must be weak to prevent energy transfer via collective spin modes. In our case, the estimated Gd−Gd coupling yields $J_{ij}/k_BT \approx 10^{-3}$−$10^{-4}$ indicating that

https://doi.org/10.1021/acsami.5c06002
ACS Appl. Mater. Interfaces XXXX, XXX, XXX−XXX

collective excitations are indeed unlikely; (ii) the wavelength of the trapped phonon must be significantly longer than the average spin separation, i.e., $k_0 d_{av} \ll 1$. For ***m*CB-Gd**, considering $\Delta_H/k_B \approx 1.9$ K at 0.2 T and the Debye approximation, $h\nu_0 = c_s k_0$ with the typical solid sound velocity of $c_s \approx 5 \times 10^3$ m/s yields, $k_0 \approx 8 \times 10^6$ m^{-1} and since the average distance between Gd centers is $d_{av} \approx 9.5$ Å, considering both intra- and interchain distances, we obtain $k_0 d_{av} \approx 7.6 \times 10^{-3}$, fulfilling the condition for RPT. The extracted τ_3 values also agree with those previously reported for RPT processes in Gd compounds.[71,75] Although a Raman mechanism can exhibit a $\tau^{-1} \propto T^2$ dependence under certain conditions,[76] it is unlikely here, as the 4−10 K range where τ_3 is observed lies well below the Debye temperature of ***m*CB-Gd**, $\Theta_D \approx 210 \pm 10$ K, estimated from specific heat data (see Figure S3).

It is noted that, below 4 K, τ_3^{-1} increases as temperature decreases, following a $\tau^{-1} \propto T^{-k}$ trend ($k \approx 0.8$). This reciprocating-thermal behavior with $k \approx 0.5-1$ has been previously observed in other Gd,[55,77] RE and transition-metal compounds,[78] and has been tentatively attributed to a secondary solution of the phonon-bottleneck equations.[79]

Heat Capacity and Magnetocaloric Effect. The thermal properties of ***m*CB-Gd** were investigated by heat capacity (HC) measurements across a temperature range of 0.3−30 K under magnetic fields varying from 0 to 3 T (Figure 4a). The magnetic contribution to the specific heat, $C_m(T, H)$, was determined by subtracting the lattice contribution, $C_L = AT^n$ (Figure 4b). At zero field, $C_m(T)$ exhibits a broad Schottky-like contribution, induced by the crystal field splitting of the Gd(III) levels, which shifts to higher temperatures for increasing magnetic fields. No signs of AF ordering were observed down to the lowest measured temperature of 0.35 K. The experimental data are well reproduced by theoretical $C_m(T, H)$ curves, calculated with *Phi* code considering the ab initio-derived single-ion D, E parameters for the three Gd(i) sites and J_{ij} constants (Table Figure 5a).

(a)

Gd(i)	D (cm^{-1})	E (cm^{-1})	Interaction	J_{ij} (cm^{-1})
Gd1	0.057	0.000	Gd1-Gd2	J_{12} =+0.0038
Gd2	0.082	-0.012	Gd2-Gd3	J_{23} = -0.0042
Gd3	0.038	-0.006	Gd3-Gd1	J_{13} = -0.0021

(b)

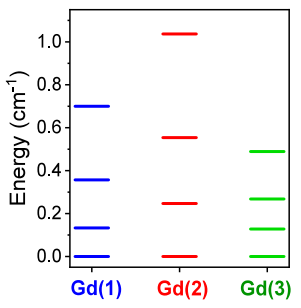

Figure 5. (a) Ab initio-calculated axial (D) and orthorhombic (E) anisotropy parameters of the ZFS tensor for the three nonequivalent sites for Gd(III) ions in ***m*CB-Gd**, and intrachain n.n. magnetic interactions, within a Hamiltonian $\widehat{\mathcal{H}}_{ex} = -2\sum J_{ij}\vec{S}_i \cdot \vec{S}_j$ (here $J_{ij} < 0$ denotes AF coupling). (b) Calculated energy levels of the ground state for the three distinct Gd(i) coordination sites in zero applied magnetic field.

The magnetocaloric effect (MCE) performance was evaluated from the HC data. Figure 4c shows the magnetic entropy change $-\Delta S_m(T, \Delta B)$ for selected field changes $\Delta B = (0 - B_f) = 0.5$, 1, 2 T. For practical purposes, it is relevant to discuss results obtained for $B_f = 2$ T, as this field can be easily achieved using permanent magnets in magnetic refrigerator applications. At $\Delta B = 2$ T, the maximum magnetic entropy change is $-\Delta S_m{}^{max} = 4.67$ R (24.14 mJ cm^{-3} K^{-1}) at $T_{max} = 0.79$ K, which is a 75% of the systems' total available magnetic entropy, $S_{max} = 3\text{Rlog}(2S + 1) = 6.24$ R. Additionally, the adiabatic temperature change $\Delta T_{ad}(T) = T_f - T_i$ was determined (Figure 4d). For $\Delta B = 2$ T, the temperature decrease reaches a maximum of $\Delta T_{ad}^{max} = 5.61$ K at $T = 1.22$ K. The full width at half-maximum of the $-\Delta S_m$ curve is $\delta T_{fwhm} = 2.14$ K, yielding a relative cooling power of RCP = $-\Delta S_m{}^{max} \times \delta T_{fwhm} = 51.7$ mJ cm^{-3}. The MCE performance at higher applied magnetic fields, up to 5 T, was further evaluated using magnetization vs field data collected at various temperatures (Figure 2b), applying the Maxwell method.[26] For $\Delta B = 5$ T, the magnetic entropy change reaches 5.88 R, that is, 94.3% of the system's maximum available entropy (Figure 4c).

Ab Initio Calculations. The ground state of the free Gd(III) ion is in a first approximation a pure $^8S_{7/2}$ multiplet ($L = 0$, $S = 7/2$), which is spherically symmetric, i.e. isotropic under an external field. However, spin−orbit coupling also produces a small mixing of the ground state octet with the excited sextets or even higher energy multiplets. This mixing, in combination with crystal field effects, gives rise to a zero-field splitting (ZFS) of the ground state multiplet into four Kramers doublets.[80] The distortion of the coordination atoms around Gd thus determines the actual electronic level scheme. Ab initio calculations, using the CASSCF/RASSI-SO method,[81,82] were performed to determine the axial and orthorhombic anisotropy parameters, along with the energy levels for the fundamental multiplet, for the three distinct Gd(i) sites in ***m*CB-Gd** MOF. The Hamiltonian describing the single-ion level splitting for each Gd(i) under an applied magnetic field is given by

$$\widehat{\mathcal{H}}_i = D_i S_{zi}^2 + E_i(S_{xi}^2 - S_{yi}^2) - g\mu_B \vec{S}_i \cdot \vec{B} \quad (1)$$

where D_i and E_i represent for each ion the axial and orthorhombic components of the zero-field splitting tensor producing magnetic anisotropy, and the last term accounts for Zeeman energy term with the $g \approx 2$. The total Hamiltonian operates on the complete 8-fold basis function of the unperturbed wave function $|7/2, S_z\rangle$. The calculated values of D_i, E_i are summarized in Figure 5a. For the three coordination environments, Gd is predicted to exhibit planar anisotropy ($D > 0$), indicating that the z-axis is the hard magnetization axis. Gd(2) displays the largest anisotropy value ($D_2 = 0.082$ cm^{-1}), differing by 54% from the smallest value calculated for Gd(3). Additionally, we calculated the nearest-neighbor magnetic interactions between the three Gd(i) ions within a chain by applying the Broken Symmetry DFT method, as detailed in the Experimental Section.[83] The coupling interaction constants, described by an interaction Hamiltonian of the form $\widehat{\mathcal{H}}_{ex} = -2\sum J_{ij}\vec{S}_i \cdot \vec{S}_j$ are also given in Figure 5a.

At sufficiently low temperatures, the system can be described by the fundamental multiplet formed by the four lowest Kramers doublets (KDs). The ab initio calculated energy levels and components of the gyromagnetic tensor under pseudospin

https://doi.org/10.1021/acsami.5c06002
ACS Appl. Mater. Interfaces XXXX, XXX, XXX−XXX

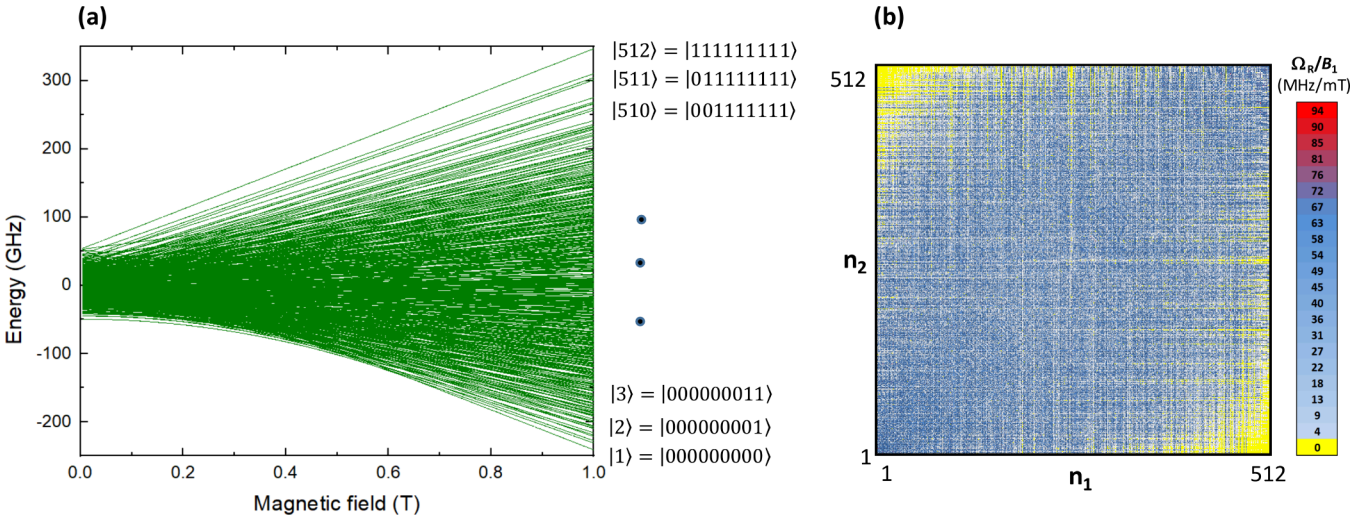

Figure 6. 512-level qudit implemented in ***m*CB-Gd** quMOF. (a) Energy level scheme calculated using *Phi* suite and ab initio-derived parameters at 3.6 K with the magnetic field applied in the *z*-direction. (b) Color map of the Rabi frequencies induced by B_1-driven resonant transitions between adjacent levels, calculated at 0.6 T (along the *z*-axis).

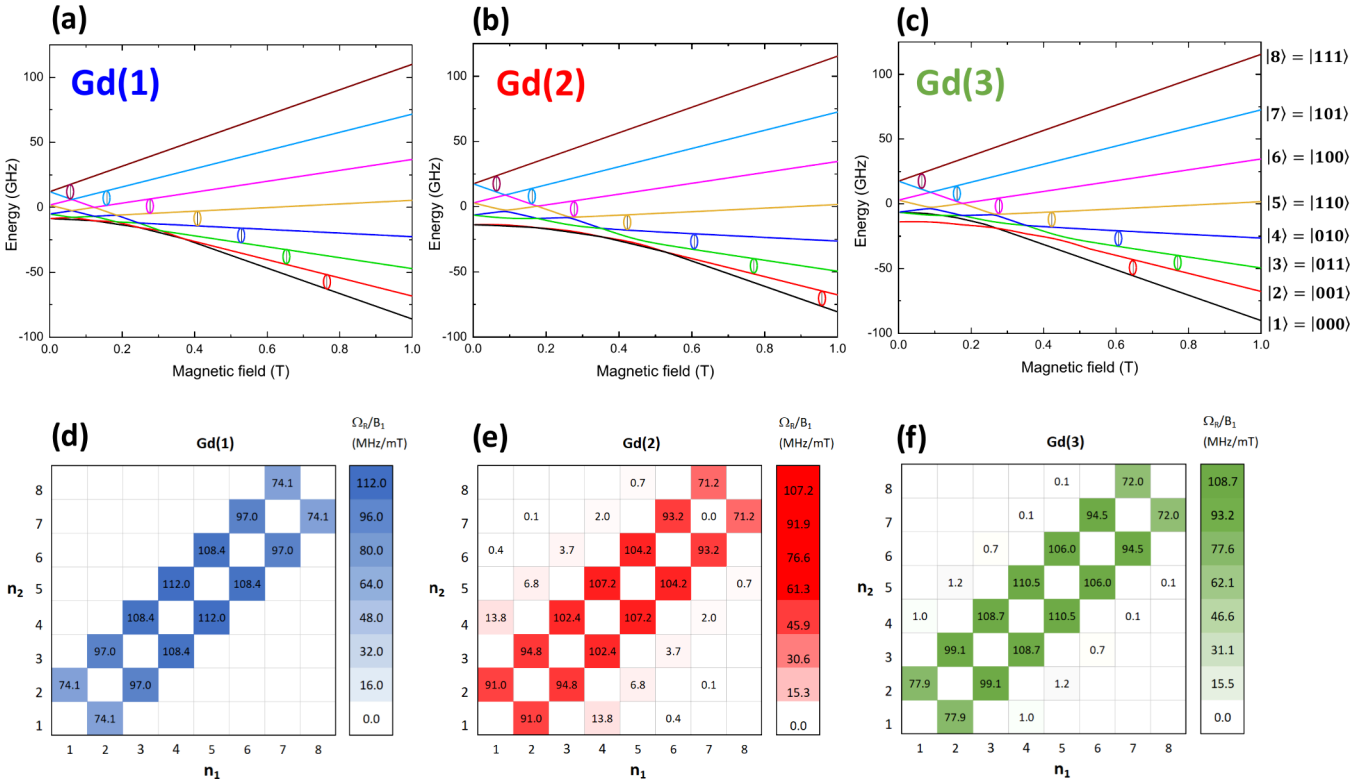

Figure 7. Three isolated 8-level qudits. (Top) Energy level scheme calculated using *Phi* suite and ab initio-derived parameters at 3.6 K with *H*//z for (a) Gd(1), (b) Gd(2), (c) Gd(3) in magnetically diluted *m*CB-Gd_yY_{100-y} MOFs, behaving as 8-level qudits. (Bottom) Rabi frequencies (normalized by B_1) calculated at 0.6 T (along the *z*-axis) for each Gd(*i*) (d–f).

(g_x*, g_y*, g_z*) of these four KDs for the three different Gd(*i*) coordination sites are summarized in Figure 5 and Table S1.

As demonstrated in previous sections, the experimental magnetization, susceptibility (Figure 2a,b) and heat capacity (Figure 4b) data could be well described by *Phi* calculations within a Hamiltonian encompassing the ab initio-calculated parameters, confirming the validity of the model.

To evaluate the potential of this triple-site Gd_3 quMOF for Quantum Computing, we calculated its energy level scheme under an applied field using *Phi* software, incorporating the ab initio-derived D_i, E_i and J_{ij} parameters. As shown in Figure 6a, the calculated energy level scheme at 3.6 K, mapped as a function of the magnetic field up to $\mu_0 H$ = 1 T, reveals 512 separated states, sufficient to encode up to N = 9 qubits. This finding highlights the system's capacity to address scaling challenges in Quantum Computing.

An important aspect to note is that this quMOF would admit quantum universal operations,[41] implying that any quantum superposition of the 512-dimension Hilbert space can be generated from any initial state through the application of a

https://doi.org/10.1021/acsami.5c06002
ACS Appl. Mater. Interfaces XXXX, XXX, XXX−XXX

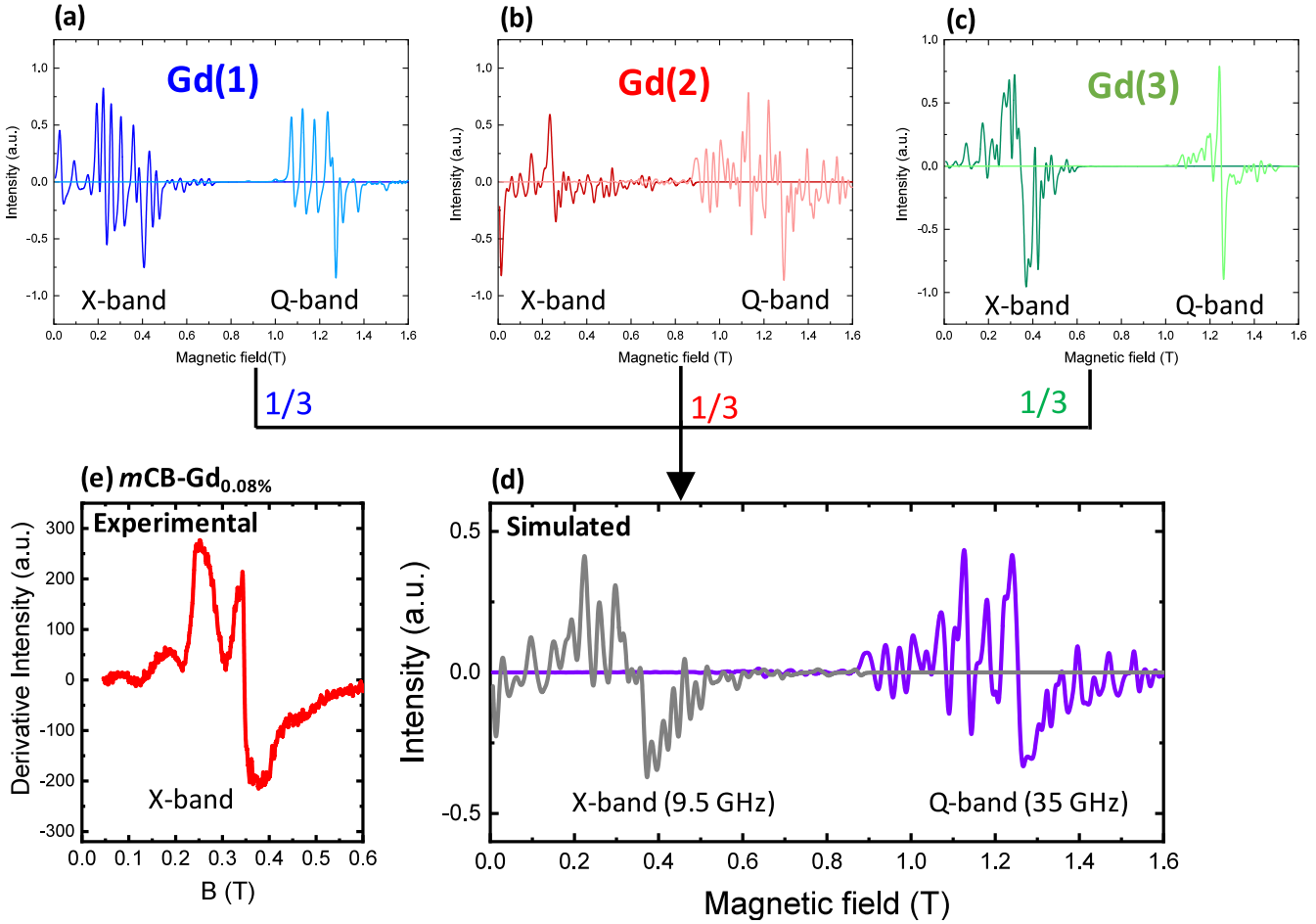

Figure 8. CW-EPR spectra of Gd(i) sites and diluted GdY quMOF. (Top) Continuous-wave EPR (CW-EPR) spectra at X-band (9.5 GHz) and Q-band (35 GHz) at 3.6 K for the three distinct Gd(i) sites in ***m*CB-Gd** quMOF, (a) Gd(1), (b) Gd(2), and (c) Gd(3), calculated using *Phi* with ab initio-derived D_i, E_i parameters. (d) Simulated CW-EPR spectra for a magnetically diluted *m*CB-GdY MOF, assuming an equimolar contribution from all three isolated Gd(i) sites. (e) Experimental X-band spectrum for the ***m*CB-Gd$_{0.08\%}$** sample.

sequence of electromagnetic pulses. This capability arises from the existence of allowed transitions between the different spin levels, which can be selectively addressed by tuning the frequency of the pulse or adjusting the external magnetic field. The condition of universality for ***m*CB-Gd** quMOF is demonstrated in Figure 6b, where we plot the Rabi frequencies (normalized by the driving field B_1) calculated at an intermediate field 0.6 T linking the different levels, numbered from 1 to 512. The dense map of allowed transitions makes it possible to access any final state by concatenating successive $(n_i - n_{i+1})$ resonant transitions at different frequencies.

It is noted that the crowding of the states would impede coherent manipulation of this qudit using conventional X-band technology, typically operating at microwave frequencies (~10 GHz). However, ongoing developments in L-band (1 GHz) EPR[84,85] may provide the fine spectral resolution needed to resolve these closely spaced transitions. Moreover, emerging broadband spectroscopy instrumentation[86] offers promising potential to enable tailored multifrequency manipulation of large-dimensional qudits.[87]

Additionally, the magnetically diluted *m*CB-GdY MOFs contain isolated Gd ions in 3 distinct coordination sites, each capable of functioning as an 8-state qudit. To illustrate this, we simulated the field-split energy level scheme for each Gd(i) site using ab initio-derived E_i, D_i parameters. Figure 7a–c demonstrates that all three Gd(i) sites exhibit 8 well-separated energy levels, with 7 transitions that would be accessible via standard X-band EPR at 10 GHz. Furthermore, the condition of universality is satisfied for each of the three 8-level qudits, as evidenced by the calculated Rabi frequencies at 0.6 T along the z-axis for each Gd(i) ion (Figure 7d–f). Additional data, including calculated Rabi frequencies for other magnetic field orientations and values, are provided in the Supporting Information (S5).

Pulsed EPR quMOF Characterization. Pulsed EPR measurements were conducted on two quMOFs with different percentage of magnetic dilution, ***m*CB-Gd$_{0.08\%}$** and ***m*CB-Gd$_{1.76\%}$**. The echo-detected field-swept (ES-EPR) X-band EPR spectra (9.5 GHz) of the two powdered samples at 6 and 10 K are presented in Figure S8. The X-band continuous wave (CW) EPR spectrum for the most diluted sample (***m*CB-Gd$_{0.08\%}$**) at 3.6 K, derived from the first derivative of the ES-EPR spectrum, is presented in Figure 8e. In this sample, the magnetic interactions between Gd ions are negligible due to the high dilution. The experimental CW-EPR spectrum closely matches the theoretical prediction, which was obtained as a weighted linear combination of the spectra corresponding to the three distinct Gd(i) sites (i = 1, 2, 3), shown in Figure 8d. These individual spectra were calculated using *Phi* suite, with zero-field splitting parameters (D_i, E_i) derived from ab initio

https://doi.org/10.1021/acsami.5c06002
ACS Appl. Mater. Interfaces XXXX, XXX, XXX−XXX

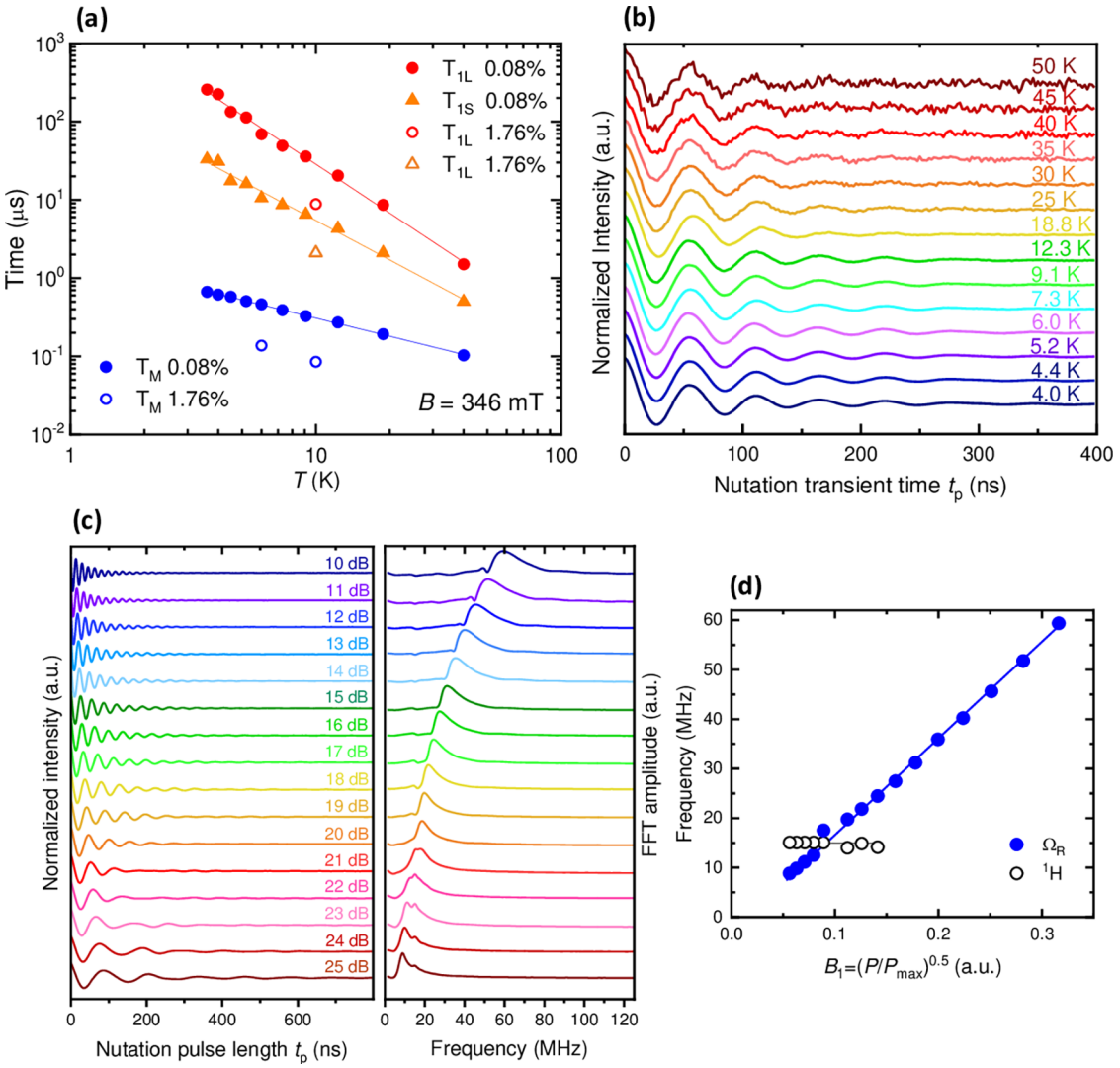

Figure 9. Pulsed EPR of *m*CB-GdY quMOFs. (a) Temperature-dependence of T_1 and T_m obtained at 346 mT for magnetically diluted samples ***m*CB-Gd**$_{0.08\%}$ and ***m*CB-Gd**$_{1.76\%}$. (b) Rabi oscillations for ***m*CB-Gd**$_{0.08\%}$ at 346 mT for different temperatures between 4−50 K. (c) Nutation experiments on ***m*CB-Gd**$_{0.08\%}$ at 3.6 K for different M_w attenuation values in dB, and (right) Fast Fourier Transform (FFT). (d) Rabi frequencies obtained from FFT as a function of the microwave field B_1.

(Figure 8a−c). The excellent agreement between the experimental and theoretical spectra demonstrates the reliability of the ab initio-derived parameters.

Pulsed EPR experiments were conducted between 3.6 and 50 K on the two magnetically diluted ***m*CB-Gd**$_y$ (y = 0.08%, 1.76%) MOFs to investigate qubit spin dynamics. The spin−lattice relaxation time T_1 was determined using a standard inversion recovery sequence (see Experimental Section). Inversion recovery data were collected at different temperatures within this range, both at the field position corresponding to the maximum of the field-swept echo-detected spectra, as well as at other lateral field positions (Figure S9). Experimental data were fit with a biexponential function, Eq. (2), yielding a short ($T_{1,s}$) and a long ($T_{1,L}$) spin−lattice relaxation times.

The phase-memory time T_m was determined using a Hahn spin echo decay sequence, and the echo intensity data was fit to a single-exponential function, Eq. (3). T_1 and T_m were measured at the field position corresponding to the maximum (B = 346 mT) of the field-swept echo-detected spectra across 3.6−40 K for ***m*CB-Gd**$_{0.08\%}$ and 6−10 K for ***m*CB-Gd**$_{1.76\%}$. Experimental data and corresponding fit parameters for $T_{1,s}$, $T_{1,L}$ are provided in Figure S9/Table S3 (***m*CB-Gd**$_{0.08\%}$) and Figure S10/Table S4 (***m*CB-Gd**$_{1.76\%}$), while those for T_m are in Figure S11/Table S5 (***m*CB-Gd**$_{0.08\%}$) and Figure S12/Table S6 (***m*CB-Gd**$_{1.76\%}$).

The temperature dependence of T_1 and T_m for both quMOFs is shown in Figure 9a. As expected, the most diluted sample (***m*CB-Gd**$_{0.08\%}$) displays longer relaxation times. At the lowest tested temperature (3.6 K), the spin−lattice relaxation times reach $T_{1,s}$ = 33 μs and $T_{1,L}$ = 256 μs. The phase memory time is T_m = 0.7 μs, comparable to previously reported values for other Gd-based quMOFs.[53] T_1 displays a stronger temperature dependence, following a stronger power-law dependence ($T_{1L} \propto T^{2.08}$, $T_{1S} \propto T^{1.68}$), compared to $T_m \propto T^{0.77}$. Although T_m remains significantly shorter than T_1 across the full temperature range, an analysis of the decoherence contributions —considering spin−lattice relaxation, electronic spectral diffusion (SD), electron spin-flop, nuclear SD and instantaneous diffusion (ID) — reveals that T_m is still indirectly limited by T_1 through the dominant electronics SD contribution (see details in Figure S13).

https://doi.org/10.1021/acsami.5c06002
ACS Appl. Mater. Interfaces XXXX, XXX, XXX−XXX

Nutation experiments were performed on the most diluted quMOF, ***m*CB-Gd$_{0.08\%}$**. These measurements were conducted at the maximum of the ES-EPR spectrum (346 mT) over a range of MW powers (10−25 dB) and temperatures (3.6−50 K). As shown in Figure 9b, nutation experiments reveal clear Rabi oscillations at all temperatures up to 50 K.

For measurements at 3.6 K, a decrease in the nutation frequency with increasing attenuation (i.e., lower MW field B_1) was observed (Figure 9c). The Fast Fourier Transform (FFT) of these data reveals a Rabi oscillation frequency (Ω_R), which increases linearly with B_1 (Figure 9d), demonstrating feasible coherent manipulation via X-band EPR. For the maximum B_1 (lowest attenuation value, 10 dB), the Rabi frequency is $\Omega_R \approx$ 60 MHz. Additionally, a field-independent peak is observed at 15.07 MHz, assigned to the Larmor frequency of ^{1}H.

To better interpret these results, we calculated the expected normalized Rabi frequencies (Ω_R/B_1, in MHz/mT) between adjacent levels ($n_i - n_j$) for the three Gd(i) ions under the experimental field of B = 346 mT, applied along both the z and y directions (Figure S6). The Ω_R/B_1 maps reveal that for the principal $-1/2 \leftrightarrow +1/2$ transition ($n_1 = 4 \rightarrow n_2 = 5$) at the Gd(1) and Gd(3) sites with $H//z$, the expected values are $\Omega_R/B_1 \approx$ 112−105.7 MHz/mT. Assuming $B_1 \approx$ 0.54 mT at 10 dB in our setup (consistent with the 0.2−0.6 mT range reported for the same equipment under similar conditions using free-electron systems), the theoretical Rabi frequency is $\Omega_R \approx$ 60.4−57.1 MHz (Figure S6), in good agreement with the experimental value.

CONCLUSIONS

The reported Gd(III) carborane-based metal−organic framework $\{[(Gd)_3(m\text{CB-L})_4(NO_3)(DMF)_x]_n\cdot Solv\}$, featuring three distinct coordination sites, represents a versatile multifunctional molecular material with exciting potential for Quantum Computing and magnetic refrigeration applications.

The static magneto-thermal properties of Gd(III) MOF, measured down to 0.35 K, were accurately modeled considering the site-specific anisotropy parameters and coupling interactions determined by ab initio calculations. Ac susceptibility measurements reveal spin−lattice magnetic relaxation associated to three mechanisms among which Rapid Phonon Trapping. Moreover, Gd(III) MOF exhibits a notable magnetocaloric effect (MCE). In fact, leveraging the optimal MCE of Gd(III) and the ability of carborane linkers to form multimetallic frameworks, we recently demonstrated the creation of multifunctional, "self-refrigerated" GdLn (Ln = Dy, Tb, Eu, Eu/Tb) mixed[69] MOFs, further broadening the application scope. Interestingly, the magnetic properties remain unaltered upon surface deposition, as demonstrated by XAS-XMCD, highlighting its potential for device integration and on-chip cooling technologies.

The use of MOFs with distinct Ln(III) coordination environments provides a new strategy to tackle the scalability challenge in Quantum Computing. The reported ***m*CB-Gd** carborane-based quMOF, with three distinct coordination sites for Gd, represents a large dimensionality 512-state qudit, which, under appropriate conditions can simulate either a 9-qubit processor, or three decoupled 8-level qudits, offering significant potential for quantum operations. Qubit characterization via pulsed EPR in a magnetically diluted (y = 0.08%) GdY MOF revealed a phase-memory time of T_m = 0.7 μs at 3.6 K and robust Rabi oscillations up to 50 K. These findings position this Gd quMOF as a promising multifunctional platform capable of supporting quantum operations across a broad temperature range.

Looking ahead, future research should focus on achieving coherent manipulation of this 512-qudit quMOF through advanced EPR instrumentation. Additionally, the presence of multiple, distinct 8-level qudits within the framework provides an opportunity to explore parallel quantum computing, potentially enabling more complex quantum algorithms and enhanced computational power.

EXPERIMENTAL SECTION

Synthesis. All chemicals were of reagent-grade quality. They were purchased from commercial sources and used as received. 1,7-di(4-carboxyphenyl)-1,7-dicarba-*closo*-dodecaborane ligand ($m\text{CBH}_2\text{L}$) was synthesized by a slight modification of a literature procedure.[88] $\{[(Gd)_3(m\text{CB-L})_4(NO_3)(DMF)_x]_n\cdot Solv\}$ (***m*CB-Gd**) was synthesized following a previously described procedure.[67] The two magnetically diluted MOFs, $\{[(Gd_yY_{100-y})_3(m\text{CB-L})_4(NO_3)(DMF)_x]_n\cdot Solv\}$, with y = 0.08 (***m*CB-Gd$_{0.08\%}$**) and y = 1.76 (***m*CB-Gd$_{1.76\%}$**), were synthesized following the same procedure but using stock methanol solutions of $Y(NO_3)_3\cdot 6H_2O$ (0.04 M) and $Gd(NO_3)_3\cdot 6H_2O$ (0.01 M) instead of the solid salts for greater accuracy. ***m*CB-Gd$_{0.08\%}$**, ICP(wt %): Gd(0.02 ± 0.005), Y(13.7 ± 0.05). ***m*CB-Gd$_{1.76\%}$**, ICP(wt %): Gd(0.37 ± 0.005), Y(11.7 ± 0.05). The samples were only air-dried and no activation was carried out prior to magnetometry.

Structural Characterization. Powder X-ray Diffraction (PXRD) was recorded at room temperature on a Siemens D-5000 diffractometer with Cu Kα radiation (λ = 1.5418 Å, 35 kV, 35 mA, increment = 0.02°). Inductively Coupled Plasma−Mass Spectrometry (ICP-MS) measurements for GdY mixed MOFs were carried out in an Agilent ICP-MS 7700x apparatus.

Magneto-Thermal Characterization. Dc magnetometry measurements in the temperature range 1.8 to 300 K were collected using a Quantum Design MPMS SQUID equipped with a 5 T magnet. Experiments were conducted on a powder sample of ***m*CB-Gd** embedded in Daphne oil to prevent grain orientation. Ac susceptibility measurements in the range between 1.8−9.0 K, at $\mu_0 H_{ac} = 4.1 \times 10^{-4}$ T, $\mu_0 H_{dc}$ = 0−2.5 T in the range of frequencies between f = 0.1−1000 Hz were determined in the same SQUID magnetometer. Furthermore, measurements in the frequency range between f = 100−10000 Hz were carried out in a Quantum Design PPMS susceptometer. Additional $M(H)$ measurements at 0.4 K were conducted in a Quantum Design MPMS3 magnetometer equipped with a ^{3}He refrigerator.

Heat capacity measurements as a function of the temperature were performed between 0.3−300 K at different applied fields between 0−3 T on a pressed powder pellet fixed with Apiezon N grease, using a Quantum Design PPMS equipped with a ^{3}He refrigerator.

XAS-XMCD. X-ray absorption spectroscopy (XAS) and X-ray magnetic circular dichroism (XMCD) experiments across the $M_{4,5}$ edge of Gd were performed at BOREAS beamline in ALBA synchrotron. For ***m*CB-Gd** a powdered sample was crashed on an indium foil and placed at the top of the coldfinger. Measurements were performed at 4.0 K ± 0.5 K. In addition, a methanol suspension of ***m*CB-Gd** crystallites was deposited by drop-casting on a Si substrate. Optical microscopy images of the deposited ***m*CB-Gd**/Si crystallites were collected by a Olympus BX51 Microscope. For XAS-XMCD measurements the sample was glued with silver paint to the sample holder, and sample temperature was 4.6 K ± 0.5 K. All spectra were recorded using Total Electron Yield (TEY) detection mode, with a 90% circularly polarized light. The XMCD ($\mu^- - \mu^+$) and XAS ($\mu^+ + \mu^-/2$) spectra at 6 T were determined from eight X-ray absorption spectra measured under right-handed (μ^+) and left-handed (μ^-) circular polarizations. XMCD(H) cycles were performed by following the resonant M_5 peak while sweeping the magnetic field between 6 and −6 T at a rate of 2 T/min.

https://doi.org/10.1021/acsami.5c06002
ACS Appl. Mater. Interfaces XXXX, XXX, XXX−XXX

Pulsed EPR. Pulsed Electron Paramagnetic Resonance (EPR) experiments were performed with a Bruker ELEXSYS 580 spectrometer operating at X-band (ca. 9.7 GHz) at the Instituto de Nanociencia y Materiales de Aragón (INMA). The spectrometer was equipped with a Bruker MD5 resonator fitted in a helium gas-flow cryostat from Oxford Instruments. Temperature control was exerted using a MercuryTC device, also from Oxford Instruments. Echo-Detected EPR experiments were obtained by acquiring the integrated intensity of a Hahn echo while sweeping the external magnetic field. For representation purposes, some of these absorption-like spectra were pseudomodulated in silico and compared to the corresponding simulation. EPR spectra were calculated using *Phi* suite, using zero-field splitting parameters for each Gd(i = 1, 2, 3) site that were obtained from the ab initio calculations.

Spin−lattice relaxation time T_1 was determined with a standard inversion recovery sequence ($\pi/2 - t - \pi/2 - \tau - \pi - \tau -$ echo) for variable t and pulse lengths $t_{\pi/2}$ = 16 ns and t_π = 32 ns. Echo inversion recovery data were collected at different temperatures between 3.6 and 50 K at the maximum of the field-swept EPR spectrum (B = 346 mT for ***m*CB-Gd$_{0.08\%}$**, B = 358 mT for ***m*CB-Gd$_{1.76\%}$**), as well as at other lateral field positions. The experimental data were fit with the biexponential function:

$$I(t) = A\exp(-t/T_{1,L}) + B\exp(-t/T_{1,S}) + y_0 \quad (2)$$

where $T_{1,s}$ and $T_{1,L}$ stand for a short and long spin−lattice relaxation times, and A and B are negative coefficients.

The phase memory time T_m was determined using a Hahn spin echo decay sequence ($\pi/2 - \tau - \pi - \tau -$ echo), fitting the echo decay time-trace to the following equation:

$$I(2\tau) = A\exp(-2\tau/T_m) + y_0 \quad (3)$$

We note that, because our Hahn-echo experiments probe an ensemble of spins, the observed echo decay constant corresponds to the phase-memory time T_m, which encompasses both homogeneous spin−spin relaxation (T_2) and additional dephasing processes (spectral diffusion, instantaneous diffusion, and unresolved inhomogeneities). Nutation experiments were performed for ***m*CB-Gd$_{0.08\%}$** using the pulse sequence $t_p - T - \pi/2 - t - \pi - t -$ echo, where t_p is the nutation pulse of variable length, which was gradually increased during the experiment between 0 to 0.9 μs in steps of 2 ns, and T = 112 ns. Several nutation experiments were performed at different power of the nutation pulse, while the detection pulses $\pi/2$ and π were optimized for each microwave power, and a two-step phase cycle was applied on the $\pi/2$ detection pulse. Integration was performed over the whole echo to eliminate off-resonance contributions.

Ab Initio Calculations. The single-ion magnetic anisotropy parameters and Gd(III) energy levels were computed using the CASSCF/RASSI-SO multireference wave function method[81,82] as implemented in the Molcas 8.6 package.[89] The atomic positions for the molecular fragments in the calculations were derived from the X-ray crystal structure of the isostructural Tb(III) derivative. The cluster models include the Gd(III) ion under study, two paramagnetic Y(III) ions placed at the positions of the two nearest Gd(III) ions, and all ligands surrounding the Gd(III) ion. In these models, the carborane linkers were replaced with benzoate ions. Additionally, the ligands coordinating to the two closest Gd(III) ions were also included, with DMF ions simplified to formaldehyde and carborane linkers to formate ions. All atoms were represented using basis sets of atomic natural orbitals from the ANO RCC library.[90] The following basis sets were employed: VQZP for the Gd ion, VTZP for the O, C, and N atoms within the first three coordination shells around the Gd ion, and VDZ for all other atoms.

A CASSCF active space with 7 electrons in the 7 Gd 4f orbitals (CAS(7,7)) was used to compute 1 octet and 48 sextets. The RASSI-SO calculations were performed using the AMFI approximation[91] for spin−orbit coupling, with relativistic effects treated using the DKH2 Douglas-Kroll Hamiltonian.[92] Finally, the SINGLE_ANISO module[89] was employed to calculate the effective spin Hamiltonian parameters for the Gd(III) ground state multiplet.

The magnetic coupling constants were calculated using the Yamaguchi's DFT Broken-Symmetry approach,[83] as implemented in the Orca 6.0 package.[93,94] The molecular fragments consisted of the two interacting Gd(III) ions, with the nearest Gd(III) ions replaced by Y(III) ions, along with all ligands coordinated to these four Gd(III) ions, applying the same simplifications as in the CASSCF/RASSI-SO calculations. The DFT calculations were carried out using the B3LYP[95,96] functional and the following basis sets: SARC-DKH-TZVP[97] for the Gd(III) and Y(III) ions, and DKH-def2-TZVP[98] for all other atoms, both of them including scalar relativistic effects. To speed up the calculations the SARC/J auxiliary basis[97] along with the resolution of identity (RI)[99] and the chain-of-spheres (COSX)[100] approximations were used.

■ ASSOCIATED CONTENT

Supporting Information

The Supporting Information is available free of charge at https://pubs.acs.org/doi/10.1021/acsami.5c06002.

S1, additional structural characterization; S2, XAS-XMCD of surface-deposited *m*CB-Gd MOF; S3, Debye temperature estimation; S4, ab initio calculations; S5, calculation of Rabi frequencies; and S6, EPR spectroscopy (PDF)

■ AUTHOR INFORMATION

Corresponding Authors

Elena Bartolomé − *Consejo Superior de Investigaciones Científicas (CSIC), Institut de Ciència de Materials de Barcelona (ICMAB), 08193 Barcelona, Spain;* orcid.org/0000-0001-5108-0977; Email: ebartolome@icmab.es

José Giner Planas − *Consejo Superior de Investigaciones Científicas (CSIC), Institut de Ciència de Materials de Barcelona (ICMAB), 08193 Barcelona, Spain;* orcid.org/0000-0002-1648-2169; Email: jginerplanas@icmab.es

Authors

Xiao-Bao Li − *Consejo Superior de Investigaciones Científicas (CSIC), Institut de Ciència de Materials de Barcelona (ICMAB), 08193 Barcelona, Spain*

Ana Arauzo − *CSIC-Universidad de Zaragoza, and Departamento de Física de la Materia Condensada, Instituto de Nanociencia y Materiales de Aragón (INMA), 50009 Zaragoza, Spain;* orcid.org/0000-0002-5999-341X

Javier Luzón − *Centro Universitario de Defensa (CUD), 50090 Zaragoza, Spain*

Inés García-Rubio − *CSIC-Universidad de Zaragoza, and Departamento de Física de la Materia Condensada, Instituto de Nanociencia y Materiales de Aragón (INMA), 50009 Zaragoza, Spain;* orcid.org/0000-0002-1827-1250

Complete contact information is available at: https://pubs.acs.org/10.1021/acsami.5c06002

Author Contributions

Conceptualization: E.B.; project administration: E.B.; supervision: E.B., J.G.P; funding acquisition: E.B., J.G.P.; resources: X.-B.L., J.G.P., A.A., I.G.-R., E.B.; investigation: E.B., A.A., I.G.-R.; formal analysis: E.B., A.A.; methodology: J.L., E.B.; validation: I.G.-R., A.A.; visualization: E.B., J.G.P.; writing—original draft: E.B.; writing−review and editing: A.A., I.G.-R., J.G.P.

Notes

The authors declare no competing financial interest.

https://doi.org/10.1021/acsami.5c06002
ACS Appl. Mater. Interfaces XXXX, XXX, XXX−XXX

■ ACKNOWLEDGMENTS

This work was financially supported by Spanish MCIN (PID2022-138492NB-I00, PID2022-136892NB-I00 and PID2021-127287NB-I00), the Generalitat de Catalunya (2021/SGR/00442), and the Gobierno de Aragón (RASMIA E12-23, and E09-23R). E.B., J.G.P., A.A., and I.G.-R. acknowledge financial support from the State Investigation Agency, through the Severo Ochoa Programme for Centres of Excellence in R&D (CEX2023-001263-S and CEX2023-001286-S, funded by MICIU/AEI/10.13039/501100011033). The authors would like to acknowledge the use of Servicio General de Apoyo a la Investigación-SAI, Universidad de Zaragoza, and the financial support from MCIN with resources from European Union NextGeneration EU (PRTR-C17.I1) promoted by the Government of Aragón. X.-B.L. acknowledges the China Scholarship Council (CSC) for his PhD grant (202106650003). XAS and XMCD experiments were performed at the BOREAS beamline of the ALBA synchrotron with the support of ALBA staff (experiment number 2022085925).

■ REFERENCES

(1) Ladd, T. D.; Jelezko, F.; Laflamme, R.; Nakamura, Y.; Monroe, C.; O'Brien, J. L. Quantum Computers. *Nature* **2010**, *464*, 45−53.
(2) Arute, F.; Arya, K.; Babbush, R.; Bacon, D.; Bardin, J. C.; Barends, R.; Biswas, R.; Boixo, S.; Brandao, F. G. S. L.; Buell, D. A.; Burkett, B.; Chen, Y.; Chen, Z.; Chiaro, B.; Collins, R.; Courtney, W.; Dunsworth, A.; Farhi, E.; Foxen, B.; Fowler, A.; Gidney, C.; Giustina, M.; Graff, R.; Guerin, K.; Habegger, S.; Harrigan, M. P.; Hartmann, M. J.; Ho, A.; Hoffmann, M.; Huang, T.; Humble, T. S.; Isakov, S. V.; Jeffrey, E.; Jiang, Z.; Kafri, D.; Kechedzhi, K.; Kelly, J.; Klimov, P. V.; Knysh, S.; Korotkov, A.; Kostritsa, F.; Landhuis, D.; Lindmark, M.; Lucero, E.; Lyakh, D.; Mandrà, S.; McClean, J. R.; McEwen, M.; Megrant, A.; Mi, X.; Michielsen, K.; Mohseni, M.; Mutus, J.; Naaman, O.; Neeley, M.; Neill, C.; Niu, M. Y.; Ostby, E.; Petukhov, A.; Platt, J. C.; Quintana, C.; Rieffel, E. G.; Roushan, P.; Rubin, N. C.; Sank, D.; Satzinger, K. J.; Smelyanskiy, V.; Sung, K. J.; Trevithick, M. D.; Vainsencher, A.; Villalonga, B.; White, T.; Yao, Z. J.; Yeh, P.; Zalcman, A.; Neven, H.; Martinis, J. M. Quantum Supremacy Using a Programmable Superconducting Processor. *Nature* **2019**, *574* (7779), 505−510.
(3) Kjaergaard, M.; Schwartz, M. E.; Braumüller, J.; Krantz, P.; Wang, J. I.-J.; Gustavsson, S.; Oliver, W. D. Superconducting Qubits: Current State of Play. *Annu. Rev. Condens Matter Phys.* **2020**, *11*, 369−395.
(4) Loss, D.; DiVincenzo, D. P. Quantum Computation with Quantum Dots. *Phys. Rev. A* **1998**, *57*, 120−126.
(5) Monroe, C.; Kim, J. Scaling the Ion Trap Quantum Processor. *Processor Science* **2013**, *339*, 1164−1169.
(6) Madsen, L. S.; Laudenbach, F.; Askarani, M. F.; Rortais, F.; Vincent, T.; Bulmer, J. F. F.; Miatto, F. M.; Neuhaus, L.; Helt, L. G.; Collins, M. J.; Lita, A. E.; Gerrits, T.; Nam, S. W.; Vaidya, V. D.; Menotti, M.; Dhand, I.; Vernon, Z.; Quesada, N.; Lavoie, J. Quantum Computational Advantage with a Programmable Photonic Processor. *Nature* **2022**, *606*, 75−81.
(7) Gaita-Ariño, A.; Luis, F.; Hill, S.; Coronado, E. Molecular Spins for Quantum Computation. *Nat. Chem.* **2019**, *11* (4), 301−309.
(8) Chiesa, A.; Santini, P.; Garlatti, E.; Luis, F.; Carretta, S. Molecular Nanomagnets: A Viable Path toward Quantum Information Processing? *Rep. Prog. Phys.* **2024**, *87*, No. 034501.
(9) Fursina, A. A.; Sinitskii, A. Toward Molecular Spin Qubit Devices: Integration of Magnetic Molecules into Solid-State Devices. *ACS Appl. Electron Mater.* **2023**, *5*, 3531−3545.
(10) Zadrozny, J. M.; Niklas, J.; Poluektov, O. G.; Freedman, D. E. Millisecond Coherence Time in a Tunable Molecular Electronic Spin Qubit. *ACS Cent. Sci.* **2015**, *1*, 488−492.
(11) Godfrin, C.; Ferhat, A.; Ballou, R.; Klyatskaya, S.; Ruben, M.; Wernsdorfer, W.; Balestro, F. Operating Quantum States in Single Magnetic Molecules: Implementation of Grover's Quantum Algorithm. *Phys. Rev. Lett.* **2017**, *119*, No. 187702.
(12) DiVincenzo, D. P.; Loss, D. Quantum Computers and Quantum Coherence. *J. Magn. Magn. Mater.* **1999**, *200*, 202−218.
(13) Macaluso, E.; Rubin, M.; Aguila, D.; Chiesa, A.; Barrios, L.; Martinez, J.; Alonso, P.; Roubeau, O.; Luis, F.; Aromi, G.; Carretta, S. A Heterometallic [LnLn'Ln] Lanthanide Complex as a Qubit with Embedded Quantum Error Correction. *Chem. Sci.* **2020**, *11* (38), 10337−10343.
(14) Carreta, S.; Zueco, D.; Chiesa, A.; Gómez-León, A.; Luis, F. A Perspective on Scaling up Quantum Computation with Molecular Spins. *Appl. Phys. Lett.* **2021**, *118*, 240501.
(15) Rollano, V.; de Ory, M. C.; Buch, C. D.; Rubín-Osanz, M.; Zueco, D.; Sánchez-Azqueta, C.; Chiesa, A.; Granados, D.; Carretta, S.; Gomez, A.; Piligkos, S.; Luis, F. High Cooperativity Coupling to Nuclear Spins on a Circuit Quantum Electrodynamicss Architecture. *Commun. Phys.* **2022**, *5*, 246.
(16) Gimeno, I.; Kersten, W.; Pallarés, M. C.; Hermosilla, P.; Martínez-Pérez, M. J.; Jenkins, M. D.; Angerer, A.; Sánchez-Azqueta, C.; Zueco, D.; Majer, J.; Lostao, A.; Luis, F. Enhanced Molecular Spin-Photon Coupling at Superconducting Nanoconstrictions. *ACS Nano* **2020**, *14* (7), 8707−8715.
(17) Urtizberea, A.; Natividad, E.; Alonso, P. J.; Pérez-Martínez, L.; Andrés, M. A.; Gascón, I.; Gimeno, I.; Luis, F.; Roubeau, O. Vanadyl Spin Qubit 2D Arrays and Their Integration on Superconducting Resonators. *Mater. Horiz.* **2020**, *7*, 885−897.
(18) Bayliss, S. L.; Laorenza, D. W.; Mintun, P. J.; Kovos, B. D.; Freedman, D. E.; Awschalom, D. D. Optically Addressable Molecular Spins for Quantum Information Processing. *Science* **1979**, *2020* (370), 1309−1312.
(19) Moreno-Pineda, E.; Wernsdorfer, W. Measuring Molecular Magnets for Quantum Technologies. *Nat. Rev. Phys.* **2021**, *1*, 645−659.
(20) Janković, D.; Hartmann, J.-G.; Ruben, M.; Hervieux, P.-A. Noisy Qudit vs Multiple Qubits: Conditions on Gate Efficiency for Enhancing Fidelity. *npj Quantum Inf.* **2024**, *10*, 59.
(21) Luis, F.; Repollés, a.; Martínez-Pérez, M. J.; Aguilà, D.; Roubeau, O.; Zueco, D.; Alonso, P. J.; Evangelisti, M.; Camón, a.; Sesé, J.; Barrios, L. a.; Aromí, G. Molecular Prototypes for Spin-Based CNOT and SWAP Quantum Gates. *Phys. Rev. Lett.* **2011**, *107*, No. 117203.
(22) Aguilà, D.; Barrios, L. A.; Velasco, V.; Roubeau, O.; Repollés, A.; Alonso, P. J.; Sesé, J.; Teat, S. J.; Luis, F.; Aromí, G. Heterodimetallic [LnLn'] Lanthanide Complexes: Toward a Chemical Design of Two-Qubit Molecular Spin Quantum Gates. *J. Am. Chem. Soc.* **2014**, *136*, 14215−14222.
(23) Maniaki, D.; Garay-Ruiz, D.; Barrios, L. A.; Martins, D. O. T. A.; Aguilà, D.; Tuna, F.; Reta, D.; Roubeau, O.; Bo, C.; Aromí, G. Unparalleled Selectivity and Electronic Structure of Heterometallic [LnLn'Ln] Molecules as 3-Qubit Quantum Gates. *Chem. Sci.* **2022**, *13*, 5574.
(24) Ferrando-Soria, J.; Pineda, E. M.; Chiesa, A.; Fernandez, A.; Magee, S. A.; Carretta, S.; Santini, P.; Vitorica-Yrezabal, I. J.; Floriana, T.; Timco, G. A.; McInnes, E. J. L.; Winpenny, R. E. P. A Modular Design of Molecular Qubits to Implement Universal Quantum Gates. *Nat. Commun.* **2016**, *7*, No. 11377.
(25) Campbell, E. T. Enhanced Fault-Tolerant Quantum Computing in ?-Level Systems. *Phys. Rev. Lett.* **2014**, *113*, No. 230501.
(26) Lanyon, B. P.; Barbieri, M.; Almeida, M. P.; Jennewein, T.; Ralph, T. C.; Resch, K. J.; Pryde, G. J.; O'Brien, J. L.; Gilchrist, A.; White, A. G. Simplifying Quantum Logic Using Higher-Dimensional Hilbert Spaces. *Nat. Phys.* **2009**, *5*, 134−140.
(27) Hussain, R.; Allodi, G.; Chiesa, A.; Garlatti, E.; Mitcov, D.; Konstantatos, A.; Pedersen, K.; De Renzi, R.; Piligkos, S.; Carretta, S. Coherent Manipulation of a Molecular Ln-Based Nuclear Qudit Coupled to an Electron Qubit. *J. Am. Chem. Soc.* **2018**, *40* (31), 9814−9818.

https://doi.org/10.1021/acsami.5c06002
ACS Appl. Mater. Interfaces XXXX, XXX, XXX−XXX

(28) Chiesa, A.; Macaluso, E.; Petiziol, F.; Wimberger, S.; Santini, P.; Carretta, S. Molecular Nanomagnets as Qubits with Embedded Quantum-Error Correction. *J. Phys. Chem. Lett.* **2020**, *11*, 8610−8615.
(29) Wang, Y.; Hu, Z.; Hu, Z.; Sanders, B. C.; Kais, S. Qudits and High-Dimensional Quantum Computing. *Front. Phys.* **2020**, *8*, 479.
(30) Kristen, M.; Schneider, A.; Stehli, A.; Wolz, T.; Danilin, S.; Ku, H. S.; Long, J.; Wu, X.; Lake, R.; Pappas, D. P.; Ustinov, A. V.; Weides, M. Amplitude and Frequency Sensing of Microwave Fields with a Superconducting Transmon Qudit. *npj Quantum Inf.* **2020**, *6*, 57.
(31) Tacchino, F.; Chiesa, A.; Sessoli, R.; Tavernelli, I.; Carretta, S. A Proposal for Using Molecular Spin Qudits as Quantum Simulators of Light-Matter Interactions. *J. Mater. Chem. C Mater.* **2021**, *9*, 10266−10275.
(32) Chicco, S.; Allodi, G.; Chiesa, A.; Garlatti, E.; Buch, C. D.; Santini, P.; Renzi, R.; De; Piligkos, S.; Carretta, S. Proof-of Concept Quantum Simulator Based on Molecular Spin Qudits. *J. Am. Chem. Soc.* **2024**, *146*, 1053−1061.
(33) Urdampilleta, M.; Klyatskaya, S.; Ruben, M.; Wernsdorfer, W. Landau-Zener Tunneling of a Single Tb3+ Magnetic Moment Allowing the Electronic Read-out of a Nuclear Spin. *Phys. Rev. B* **2013**, *87*, No. 195412.
(34) Moreno-Pineda, E.; Godfrin, C.; Balestro, F.; Wernsdorfer, W.; Ruben, M. Molecular Spin Qudits for Quantum Algorithms. *Chemical Society Reviews.* **2018**, *47*, 501.
(35) Biard, H.; Moreno-Pineda, E.; Ruben, M.; Bonet, E.; Wernsdorfer, W.; Balestro, F. Increasing the Hilbert Space Dimension Using a Single Coupled Molecular Spin. *Nat. Commun.* **2021**, *12*, 4443.
(36) Handzlik, G.; Magott, M.; Arczyński, M.; Sheveleva, A. M.; Tuna, F.; Sarewicz, M.; Osyczka, A.; Rams, M.; Vieru, V.; Chibotaru, L. F.; Pinkowicz, D. Magnetization Dynamics and Coherent Spin Manipulation of a Propeller Gd(III) Complex with the Smallest Helicene Ligand. *J. Phys. Chem. Lett.* **2020**, *11*, 1508−1515.
(37) Buch, C. D.; Kundu, K.; Marbey, J. J.; Tol, J.; van; Weihe, H.; Hill, S.; Piligkos, S. Spin-Lattice Relaxation Decoherence Suppression in Vanishing Orbital Angular Momentum Qubits. *J. Am. Chem. Soc.* **2022**, *144*, 17597−17603.
(38) Hu, Z.; Dong, B.-W.; Liu, Z.; Liu, J.-J.; Su, J.; Yu, C.; Xiong, J.; Shi, D.-E.; Wang, Y.; Wang, B.-W.; Ardavan, A.; Shi, Z.; Jiang, S.-D.; Gao, S. Endohedral Metallofullerene as Olecular High Spin Qubit: Diverse Raby Cycles in Gd2@C79N. *J. Am. Chem. Soc.* **2018**, *140* (3), 1123−1130.
(39) Fang, Y.-H.; Liu, Z.; Wang, Y.-X.; Zhou, S.; Jiang, S.-D.; Gao, S. Orientation Mapping of Rabi Frequencies in a Rare-Earth Molecular Qudit. *Inorg. Chem. Front* **2020**, *7*, 3875.
(40) Jenkins, M. D.; Duan, Y.; Diosdado, B.; García-Ripoll, J. J.; Gaita-Ariño, A.; Giménez-Saiz, C.; Alonso, P. J.; Coronado, E.; Luis, F. Coherent Manipulation of Three-Qubit States in a Molecular Single-Ion Magnet. *Phys. Rev. B* **2017**, *95*, No. 064423.
(41) Luis, F.; Alonso, P. J.; Roubeau, O.; Velasco, V.; Zueco, D.; Aguilà, D.; Martínez, J. I.; Barrios, L. A.; Aromí, G. A Dissymmetric [Gd2] Coordination Molecular Dimer Hosting Six Addressable Spin Qubits. *Commun. Chem.* **2020**, *3* (1), 176.
(42) Inoue, M.; Yamauchi, A.; Parmar, B.; Orihashi, K.; Singh, M.; Asada, M.; Nakamura, T.; Yanai, N. Guest-Responsive Coherence Time of Radical Qubits in a Metal-Organic Framework. *ChemComm* **2024**, *60*, 6130−6133.
(43) Yamauchi, A.; Fujiwara, S.; Kimizuka, N.; Asada, M.; Fujiwara, M.; Nakamura, T.; Pirillo, J.; Hijikata, Y.; Yanai, N. Modulation of Triplet Quantum Coherence by Guest-Induced Structural Changes in a Flexible Metal-Organic Framework. *Nat. Commun.* **2024**, *15*, 7622.
(44) Sun, L.; Yang, L.; Dou, J.-H.; Li, J.; Grigorii, S.; Mardini, M.; Tan, K. O.; Chen, T.; Sun, C.; Oppenheim, J. J.; Griffin, R. G.; Dincă, M.; Tijana, R. Room-Temperature Quantitative Quantum Sensing of Lithium Ions with a Radical-Embedded Metal−Organic Framework. *J. Am. Chem. Soc.* **2022**, *144* (41), 19008−19016.
(45) Orihashi, K.; Yamauchi, A.; Inoue, M.; Parmar, B.; Fujiwara, S.; Kimizuka, N.; Asada, M.; Nakamura, T.; Yanai, N. Radical Qubits Photo-Generated in Acene-Based Metal−Organic Frameworks. *Dalton Trans* **2024**, *53*, 872−876.
(46) Yamauchi, A.; Tanaka, K.; Fuki, M.; Fujiwara, S.; Kimizuka, N.; Ryu, T.; Saigo, M.; Onda, K.; Kusumoto, R.; Ueno, N.; Sato, H.; Kobori, Y.; Miyata, K.; Yanai, N. Room-Temperature Quantum Coherence of Entangled Multiexcitons in a Metal-Organic Framework. *Sci. Adv.* **2024**, *10*, No. eadi3147.
(47) Orihashi, K.; Yamauchi, A.; Fujiwara, S.; Asada, M.; Nakamura, T.; Hui, J. K.-H.; Kimizuka, N.; Tateishi, K.; Uesaka, T.; Yanai, N. Spin-Polarized Radicals with Extremely Long Spin−Lattice Relaxation Time at Room Temperature in a Metal−Organic Framework. *J. Am. Chem. Soc.* **2023**, *145* (50), 27650−27656.
(48) Vujević, L.; Karadeniz, B.; Cindro, N.; Krajnc, A.; Mali, G.; Mazaj, M.; Avdoshenko, S. M.; Popov, A. A.; Žilić, D.; Užarević, K.; Kveder, M. Improving the Molecular Spin Qubit Performance in Zirconium MOF Composites by Mechanochemical Dilution and Fullerene Encapsulation. *Chem. Sci.* **2023**, *14*, 9389−9399.
(49) Kultaeva, A.; Pöppl, A.; Biktagirov, T. Atomic-Scale Quantum Sensing of Ensembles of Guest Molecules in a Metal-Organic Framework with Intrinsic Electron Spin Centers. *J. Phys. Chem. Lett.* **2022**, *13* (29), 6737−6742.
(50) Zadrozny, J. M.; Gallagher, A. T.; Harris, T. D.; Freedman, D. E. A Porous Array of Clock Qubits. *Journal of American Chemistry Society* **2017**, *139* (20), 7089−7094.
(51) Yu, C.-J.; Kugelgen, S.; von; Krzyaniak, M. D.; Ji, W.; Dichtel, W. R.; Wasielewski, M. R.; Freedman, D. E. Spin and Phonon Design in Modular Arrays of Molecular Qubits. *Chem. Mater.* **2020**, *32* (23), 10200−10206.
(52) Jellen, M. J.; Ayodele, M. J.; Cantu, A.; Forbes, M. D. E.; García-Garibay, M. A. 2D Arrays of Organic Qubit Candidates Embedded into a Pillared-Paddlewheel Metal−Organic Framework. *Journal of American Chemistry Society* **2020**, *142* (43), 18513−18521.
(53) López-Cabrelles, J.; Escalera-Moreno, L.; Hu, Z.; Prima-García, H.; Mínguez- Espallargas, G.; Gaita-Ariño, A.; Coronado, E. Near Isotropic D4d Spin Qubits as Nodes of a Gd(III)-Based Metal−Organic Framework. *Inorg. Chem.* **2021**, *60* (12), 8575−8580.
(54) Wang, J.; Jing, Y.; Cui, M.; Lu, Y.; Ouyang, Z.; Shao, C.; Wang, Z.; Song, Y. Spin Qubit in a 2D GdIIINaI-Based Oxamato Supramolecular Coordination Framework. *Chem.—Eur. J.* **2023**, *29*, No. e202301771.
(55) Du, X.; Sun, L. Optimizing the Spin Qubit Performance of Lanthanide/Based Metal/Organic Frameworks. *Inorg. Chem. Front* **2024**, *11*, 8660−8670.
(56) Li, Z.; Núñez, R.; Light, M. E.; Ruiz, E.; Teixidor, F.; Viñas, C.; Ruiz-Molina, D.; Roscini, C.; Planas, J. G. Water-Stable Carborane-Based Eu3+/Tb3+ Metal−Organic Frameworks for Tunable Time-Dependent Emission Color and Their Application in Anticounterfeiting Bar-Coding. *Chem. Mater.* **2022**, *34* (10), 4795−4808.
(57) Poater, J.; Viñas, C.; Bennour, I.; Escayola, S.; Solà, M.; Teixidor, F. Too Persistent to Give Up: Aromaticity in Boron Clusters Survives Radical Structural Changes. *J. Am. Chem. Soc.* **2020**, *142* (20), 9396−9407.
(58) Poater, J.; Solà, M.; Viñas, C.; Teixidor, F. π Aromaticity and Three-Dimensional Aromaticity: Two Sides of the Same Coin. *Angew. Chem.* **2014**, *53* (45), 12191−12195.
(59) Poater, J.; Viñas, C.; Solà, M.; Teixidor, F. 3D and 2D Aromatic Units Behave like Oil and Water in the Case of Benzocarborane Derivatives. *Nat. Commun.* **2022**, *13* (1), 3844.
(60) Plesek, J. Potential Applications of the Boron Cluster Compounds. *Chem. Rev.* **1992**, *92* (2), 269−278.
(61) Scholz, M.; Hey-Hawkins, E. Carbaboranes as Pharmacophores: Properties, Synthesis, and Application Strategies. *Chem. Rev.* **2011**, *111* (11), 7035−7062.
(62) Grimes, R. N. *Carboranes*; Grimes, R. N. Ed.; Academic Press, 2016.
(63) Teixidor, F.; Kaufmann, D. E. *Science of Synthesis: Houben-Weyl Methods of Molecular Transformations*, [5th ed.].; Mulzer Ed.; Georg Thieme Verlag: Stuttgart, 2015; *6*.

https://doi.org/10.1021/acsami.5c06002
ACS Appl. Mater. Interfaces XXXX, XXX, XXX−XXX

(64) Fujii, S. Expanding the Chemical Space of Hydrophobic Pharmacophores: The Role of Hydrophobic Substructures in the Development of Novel Transcription Modulators. *Medchemcomm* **2016**, *7* (6), 1082−1092.
(65) Issa, F.; Kassiou, M.; Rendina, L. M. Boron in Drug Discovery: Carboranes as Unique Pharmacophores in Biologically Active Compounds. *Chem. Rev.* **2011**, *111* (9), 5701−5722.
(66) Valliant, J. F.; Guenther, K. J.; King, A. S.; Morel, P.; Schaffer, P.; Sogbein, O. O.; Stephenson, K. A. The Medicinal Chemistry of Carboranes. *Coord. Chem. Rev.* **2002**, *232* (1), 173−230.
(67) Li, Z.; Li, X.-B.; Light, M. E.; Carrillo, A. E.; Arauzo, A.; Valvidares, M.; Roscini, C.; Teixidor, F.; Viñas, C.; Gándara, F.; Bartolomé, E.; Planas, J. G. A Metal-Organic Framework Incorporating Eight Different Size Rare-Earth Metal Elements: Toward Multifunctionality À La Carte. *Adv. Funct Mater.* **2023**, *33* (47), No. 2307369.
(68) Li, Z.; Arauzo, A.; Planas, J. G.; Bartolomé, E. Magnetic Properties and Magnetocaloric Effect of Ln = Dy, Tb Carborane-Based Metal−Organic Frameworks. *Dalton Trans.* **2024**, *53*, 8969−8979.
(69) Li, Z.; Arauzo, A.; Roscini, C.; Planas, J. G.; Bartolomé, E. Multifunctional Self-Refrigerated Multivariate {GdLn} (Ln = Dy, Tb, Tb/Eu) Metal−Organic Frameworks. *J. Mater. Chem.* **2024**, *12* (33), 21971−21986.
(70) Chilton, N. F.; Anderson, R. P.; Turner, L. D.; Soncini, A.; Murray, K. S. PHI: A Powerful New Program for the Analysis of Anisotropic Monomeric and Exchange-coupled Polynuclear *d* - and *f* -block Complexes. *J. Comput. Chem.* **2013**, *34* (13), 1164−1175.
(71) Arauzo, A.; Lazarescu, A.; Shova, S.; Bartolomé, E.; Cases, R.; Luzón, J.; Bartolomé, J.; Turta, C. Structural and Magnetic Properties of Some Lanthanide (Ln = Eu(III), Gd(III) and Nd(III)) Cyanoacetate Polymers: Field-Induced Slow Magnetic Relaxation in the Gd and Nd Substitutions. *Dalton Trans* **2014**, *43*, 12342−12356.
(72) Liu, B.; Wang, B.-W.; Wang, Z.-M.; Gao, S. Static Field Induced Magnetic Relaxations in Dinuclear Lanthanide Compounds of [Phen2Ln2(HCOO)4(HCOO)2−2x (NO3)2x] (1, Ln = Gd and x = 0.52; 2, Ln = Er and x = 0.90; Phen = 1,10-Phenanthroline). *Sci. China Chem.* **2012**, *5*, 926−933.
(73) Schenker, R.; Leuenberger, M. N.; Chaboussant, G.; Loss, D.; Güdel, H. U. Phonon Bottleneck Effect Leads to Observation of Quantum Tunneling of the Magnetization and Butterfly Hysteresys Loops in (Et4N)3Fe2F9. *Phys. Rev. B: Condens. Matter* **2005**, *72*, No. 184403.
(74) Huber, D. L. Trapping of a Resonant Phonon by a Pair of Paramagnetic Ions. *Phys. Rev. B* **1965**, *139*, No. A1684.
(75) Orendáč, M.; Sedláková, L.; Čižmár, E.; Orendáčová, a.; Feher, a.; Zhu, W. H.; Wang, Z. M.; Gao, S. Spin Relaxation and Resonant Phonon Trapping in [Gd_{2}(Fum)_{3}(H_{2}O)_{4}]·3H_{2}O. *Phys. Rev. B* **2010**, *81*, No. 214410.
(76) Shriyastava, K. N. Theory of Spin-Lattice Relaxation. *phys. status solidi b* **1983**, *117*, 437−458.
(77) Tkáč, V.; Tarasenko, R.; Doroshenko, A.; Kavečanský, V.; Čižmár, E.; Orendáčová, A.; Smolko, R.; Černák, J.; Orendáč, M. Reciprocating Thermal Behavior in a Magnetic Field Induced Slow Spin Relaxation of [Gd2(H2O)6(C2O4)3]·2.5H2O. *Solid State Sci.* **2023**, *136*, No. 107105.
(78) Rajnák, C.; Boča, R. Reciprocating Thermal Behavior in the Family of Single Ion Magnets. *Coord. Chem. Rev.* **2021**, *436*, No. 213808.
(79) Scotrt, P. L.; Jeffries, C. D. Spin-Lattice Relaxation in Some Rare-Earth Salts at Helium Temperatures; Observation of the Phonon Bottleneck. *Phys. Rev.* **1962**, *121*, 32.
(80) Wybourne, B. G. Energy Levels of Trivalent Gadolinium and Ionic Contributions to the Ground-State Splitting. *Phys. Rev.* **1966**, *148*, 317.
(81) Malmqvist, P. A.; Roos, B. O. The CASSCF State Interaction Method. *Chem. Phys. Lett.* **1989**, *155*, 189−194.
(82) Malmqvist, P. Å.; Roos, B. O.; Schimmelpfennig, B. The Restricted Active Space (RAS) State Interaction Approach with Spin-Orbit Coupling. *Chem. Phys. Lett.* **2002**, *357* (3−4), 230−240.
(83) Yamaguchi, K.; Fukui, H.; Fueno, T. Molecular Orbital (MO) Theory for Magnetically Interacting Organic Compounds. Ab-Initio MO Calculations of the Effective Exchange Integrals for Cyclophane-Type Carbene Dimers. *Chem. Lett.* **1986**, *15* (4), 625−628.
(84) Quine, R. W.; Rinard, G. A.; Ghim, B. T.; Eaton, S. S.; Eaton, G. R. A 1−2 GHz Pulsed and Continuous Wave Electron Paramagnetic Resonance Spectrometer. *Rev. Sci. Instrum.* **1996**, *67* (7), 2514−2527.
(85) Chaudhuri, U.; Mahendiran, R. Detection of L-Band Electron Paramagnetic Resonance in the DPPH Molecule Using Impedance Measurements. *RSC Adv.* **2020**, *10* (29), 17311−17316.
(86) Gimeno, I.; Urtizberea, A.; Román-Roche, J.; Zueco, D.; Camón, A.; Alonso, P. J.; Roubeau, O.; Luis, F. Broad-Band Spectroscopy of a Vanadyl Porphyrin: A Model Electronuclear Spin Qudit. *Chem. Sci.* **2021**, *12* (15), 5621−5630.
(87) Giménez-Santamarina, S.; Cardona-Serra, S.; Clemente-Juan, J. M.; Gaita-Ariño, A.; Coronado, E. Exploiting Clock Transitions for the Chemical Design of Resilient Molecular Spin Qubits. *Chem. Sci.* **2020**, *11* (39), 10718−10728.
(88) Fox, M. A. *Icosahedral Carborane Derivatives*; Durham Theses, Durham University; 1991.
(89) Aquilante, F.; Autschbach, J.; Carlson, R. K.; Chibotaru, L. F.; Delcey, M. G.; Vico, L.; De; Galván, I.; Fdez; Ferré, N.; Frutos, L. M.; Gagliardi, L.; Garavelli, M.; Giussani, A.; Hoyer, C. E.; Manni, G. L.; Lischka, H.; Ma, D.; Malmqvist, P. Å.; Müller, T.; Nenov, A.; Olivucci, M.; Pedersen, T. B.; Peng, D.; Plasser, F.; Pritchard, B.; Reiher, M.; Rivalta, I.; Schapiro, I.; Segarra-Martí, J.; Stenrup, M.; Truhlar, D. G.; Ungur, L.; Valentini, A.; Vancoillie, S.; Veryazov, V.; Vysotskiy, V. P.; Weingart, O.; Zapata, F.; Lindh, R. Molcas 8: New Capabilities for Multiconfigurational Quantum Chemical Calculations across the Periodic Table. *J. Comput. Chem.* **2016**, *37*, 506−541.
(90) Roos, B. O.; Lindh, R.; Malmqvist, P. A.; Veryazov, V.; Widmark, P.-O. New Relativistic ANO Basis Sets for Transition Metal Atoms. *J. Phys. Chem. A* **2004**, *108*, 2851.
(91) Hess, B. A.; Marian, C. M.; Wahlgren, U.; Gropen, O. A Mean-Field Spin-Orbit Method Applicable to Correlated Wavefunctions. *Chem. Phys. Lett.* **1996**, *251*, 365−371.
(92) Douglas, M.; Kroll, N. M. Quantum Electrodynamical Corrections to the Fine Structure of Helium. *Ann. Phys. (N Y)* **1974**, *82*, 89−155.
(93) Neese, F. The ORCA Program System. *Wires Comput. Mol. Sci.* **2012**, *2*, 73−78.
(94) Neese, F. Software Update: The ORCA Program System - Version 5.0. *Wiley Interdiscip. Rev.: Comput. Mol. Sci.* **2022**, *12* (1), No. e1606.
(95) Becke, A. D. Density-functional Thermochemistry. III. The Role of Exact Exchange. *J. Chem. Phys.* **1993**, *98*, 5648−5652.
(96) Lee, C.; Yang, W.; Parr, R. G. Development of the Colle-Salvetti Correlation-Energy Formula into a Functional of the Electron Density. *Phys. Rev. B Condens. Matter* **1998**, *37*, 785−789.
(97) Pantazis, D. A.; Chen, X.-Y.; Landis, C. R.; Neese, F. All-Electron Scalar Relativistic Basis Sets for Third-Row Transition Metal Atoms. *J. Chem. Theory Comput.* **2008**, *4*, 908−919.
(98) Weigend, F.; Ahlrichs, R. Balanced Basis Sets of Split Valence, Triple Zeta Valence and Quadruple Zeta Valence Quality for H to Rn: Design and Assessment of Accuracy. *Phys. Chem. Chem. Phys.* **2005**, *7*, 3297−3305.
(99) Neese, F. An Improvement of the Resolution of the Identity Approximation for the Formation of the Coulomb Matrix. *J. Comput. Chem.* **2003**, *24*, 1740−1747.
(100) Izsák, R.; Neese, F. An Overlap Fitted Chain of Spheres Exchange Method. *J. Chem. Phys.* **2011**, *135*, 144105.

https://doi.org/10.1021/acsami.5c06002
ACS Appl. Mater. Interfaces XXXX, XXX, XXX−XXX